

Article

Assessing Effectiveness of Shape Memory Alloys on the Response of Bolted T-Stub Connections Subjected to Cyclic Loading

Ahmadreza Torabipour ¹, Nima Asghari ², Homa Haghghi ^{3,*}, Shaghayegh Yaghoubi ⁴ and Girum Urgessa ³¹ Department of Civil Engineering and Water Engineering, University of Laval, Quebec, QC G1V 0A6, Canada² Department of Architectural Engineering, Pennsylvania State University, State College, PA 16801, USA³ Department of Civil, Environmental and Infrastructure Engineering, George Mason University, Fairfax, VA 22030, USA⁴ Department of Marine Engineering, Amirkabir University of Technology (Tehran Polytechnic), Tehran 1591634311, Iran

* Correspondence: hhaghghi@gmu.edu

Abstract: This study presents finite element analysis of double split tee (DST) connections with high-strength steel bolts and coupled split tee sections, to evaluate various cyclic response parameters and elements. The investigation included quantifying connection behavior and hysteretic response, damage indexes, and failure modes. Over 40 specimens were simulated in ABAQUS under cyclic loading, including shape memory alloy (SMA)-built specimens. In the post-analysis phase, the T-stub thickness, the T-stub yield strength, the bolt preload and bolt number, and the stiffener type and stiffener material for the most significant parts of the DST connection were calculated. Simulation results showed that a lower ultimate moment yielded fewer needed stem bolts. The energy dissipation (ED) capacity increased as the horizontal distance between the stem bolts decreased. Additionally, increasing the strength of the bolt and T-stub by 15% resulted in a 3.86% increase in residual displacement (RD) for the bolt and a 1.73% decrease in residual displacement for the T-stub. T-stub stiffeners enhanced ED capacity by 31.7%. SMA materials were vulnerable to mode 1 failure when used in T-stubs, bolts, or stiffeners. However, the use of SMA increased the rate of energy dissipation. Adding stiffeners to the T-stubs altered the failure indexes and improved the pattern of failure modes. In addition, stiffeners decreased the rupture and pressure indexes. As a result, the failure index of a T-stub shifted from brittle failure to ductile failure.

Keywords: SMA material; steel bolted T-stub connection; energy dissipation; failure indexes; stiffener; finite element method



Citation: Torabipour, A.; Asghari, N.; Haghghi, H.; Yaghoubi, S.; Urgessa, G. Assessing Effectiveness of Shape Memory Alloys on the Response of Bolted T-Stub Connections Subjected to Cyclic Loading. *CivilEng* **2023**, *4*, 105–133. <https://doi.org/10.3390/civileng4010008>

Academic Editors: Panagiotis Michalis, Manousos Valyrakis, Gordon Gilja and Zied Driss

Received: 29 September 2022

Revised: 21 January 2023

Accepted: 24 January 2023

Published: 30 January 2023



Copyright: © 2023 by the authors. Licensee MDPI, Basel, Switzerland. This article is an open access article distributed under the terms and conditions of the Creative Commons Attribution (CC BY) license (<https://creativecommons.org/licenses/by/4.0/>).

1. Introduction

In traditional seismic design, connections between strong columns and weak beams have been used to achieve the desired modifications to stability and cyclic behavior [1–4]. The connections also protect against soft-story occurrence via the energy dissipation (ED) mechanism [5]. However, detailing reinforcement for structural joints that must meet full-strength requirements with an over-strength factor is reported to be expensive [6–9].

Conventional T-stub connections involve welding or bolting T-stubs to the primary structural members [10]. The connection provides high flexural resistance. Both tensile and shear behaviors can be studied by deforming the top T-stub axially and transversely [11,12]. Figure 1 is an overarching illustration of how a load affects a bolted steel connection and a T-stub.

As shown in Figure 1, it is possible to develop a prying action between the T-stub flange and the support base. By preloading the T-stub bolts, a contact stress is created between the T-stub flange and the support base. Atasoy [13] and Kulak et al. [14] note that

when external loads are applied to the T-stub web, a contact pressure might be generated between the flange edge and the base. Figure 1 also shows how such contact stress would overload the T-stub bolts with a prying action force, Q , based on the flexural rigidity of the T-stub base flange. As a result of this force, the T-stub connector bolts are at risk of premature failure [15].

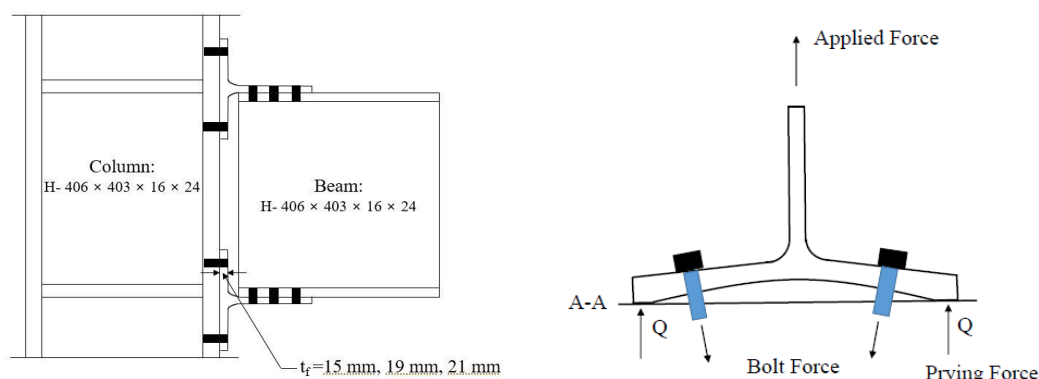


Figure 1. Bolted steel T-stub connection schematic and deformation of T-stub.

There is also an uncertainty about the position of the prying action force in the current state of the art regarding T-stub connectors. The force is assumed to act on the side line of the T-stub in a wide range of analytical models, such as those in [15–21]. AISC [16,22] and ASCE [23] have adopted this assumption.

The strength of tension zones in column flanges, end-plates, and bolts has received more attention [17]. The American Institute of Steel Construction (AISC) [24] and the Eurocode 3 [25] Standards provide analysis methods that serve as starting points from which seismic design enhancements to end-plate and T-stub connections could be derived.

Several analytical studies [18,26–31] verified static equilibrium and the application of the beam theory to the T-stub flange, and several experiments [32–34] were conducted to establish the force–displacement behavior. The T-stub connections’ rotational capacity was identified and evaluated using post-limit behavior [9,32–35], revealing the connections’ resistance and stiffness.

Abidelah et al. [36] analyzed the impact of bolts on T-stub performance and looked into the causes of failure. The functionality of a welded T-stub was studied by Barata et al. [37]. They discovered that when the temperature increased, the T-stub’s resistance and initial stiffness decreased, and its failure modes shifted.

Additionally, a three-dimensional FE model was used to study the structural behavior of the moment resisting connections and the formation of the plastic hinges in steel beam–column connections under earthquake load, and the stiffness and resistance predictions were presented in detail, with a model validated via experimental results [38,39].

For bolted T-stub connections including welded plates, the welding method is very crucial for ensuring ductile behavior of the connection [40]. T-stubs are sensitive to the minor axis of the column in out-of-plane bending [41].

High ductility in a moment resisting frame (MRF) was achieved by fabricating specimens with both unstiffened and stiffened end plate connections, with the latter using bolt extensions [42]. Diagrams illustrating the bending moment and deflection of an MRF under seismic load are shown in Figure 2.

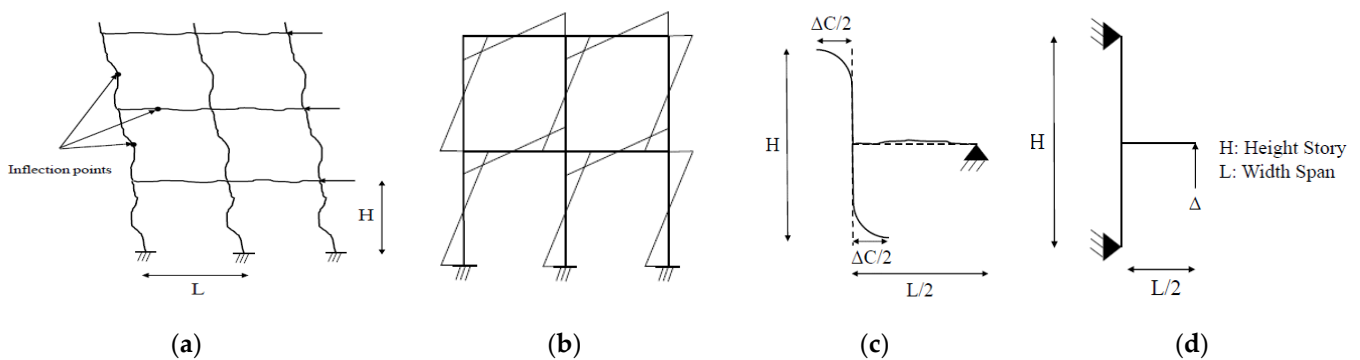


Figure 2. MRF under cyclic loading. (a) The MRF deflection diagram of the MRF, (b) moment diagram, (c) exterior connection, and (d) installed substructure in numerical modeling, reproduced with permission of Gerami et al. [43].

Ozkilic [44–47] evaluated behavior of stiffened extended end-plate connections with large bolts, application of extended end-plate connections for replaceable shear links, effects of yield line mechanisms of four bolted extended end-plate connections on frame response, and impacts of bolt diameter and end-plate thickness on capacity of connection and failure modes under cyclic and monotonic loading.

Guidelines and standards have been established by Mistakidis et al. [48], Gebbeken et al. [49], Sherbourne and Bahaari [50], Bursi and Jaspart [32,51–54], Hantouche et al. [55–59], Lemonis and Gantes [60–63], and Swanson et al. [33]. Elementary T-stubs' behavior was investigated by Soltani et al. [64] using finite element analysis. All possible modes of failure were accounted for by considering a wide range of geometry and strength characteristics. There were examples of both identical and dissimilar T-stub configurations among the specimens. To determine the full force–displacement curve of bolted connections, Fernandez-Ceniceros [65–67] has conducted extensive studies. Precise estimation of link behavior was achieved using the hybridization of FE modeling with soft-computing approaches [68].

Bravo and Herrera [69], Girao Coelho et al. [42], Hantouche et al. [59], and Herrera et al. [70] have investigated the behavior of bolted steel connections in an effort to determine their failure modes and fracture zones. As a result, bridge piers are ideal locations for conducting scour experiments [71]. The nonlinear behavior of a T-stub joint under impact stresses was also established in a study by Ribeiro et al. [72]. The force–displacement results were improved by using a ductile failure criterion, and it was found that the strain rate had an effect on the material's behavior. Different dynamic loads had little effect on the force–displacement response, despite the fact that they all applied a sizable impetus.

The finding was that an increase in bolt diameter results in an increase in plastic capacity as well as an increase in gage distance. Additionally, if the thickness of the weld increases, the plastic capacity will increase as well. Moreover, strain hardening affected the capacity of T-stub connections [73–76].

The bolted angle connection's moment rotation capacity and influencing parameter were analyzed by Saedi Daryan et al. When the shear hardness increased, the lateral drift decreased, and the frame stability increased [77].

Numerical models were developed to study the performance of the post-tensioned (PT) self-centering steel connection in the context of an intelligent seismic system. Different types of bolted angles with associated stiffeners (Shiravand et al. [78] and Abdollahzadeh et al. [79]) and SMA material [80,81] were examined for their impact on structural member behavior.

In keeping with this discovery, Asada et al. [82] described a method for increasing the plasticity of welded wide flange beam to column connections by using high-yield bolts and welding complementary H-section haunches.

Sebbagh et al. [83] found that if the flange is monotonically loaded, adding an outer row of bolts is unlikely to have any significant effect until it begins to yield. When cyclic loads are applied, the added row of bolts prevents stiffness from decreasing and can provide more than 80% more strength under cyclic loads. As a result of cyclic loading, the outer bolts take on practically all the load applied during the unloading phase while simultaneously participating in the load resistance during loading. With the addition of the outer bolts, the end part of the T-stub plate under cyclic loads is prevented from uplift, and prying forces are avoided, while the inner bolts undergo about 40% less elongation during loading and unloading.

The stainless steel T-stub to the square hollow section bolted connection was numerically studied [84]. It was shown that by increasing the flange thickness from 2 mm to 7 mm, the connection capacity was increased by 88%. Bolts positioned far apart from the stem of the T stub exhibited a ripping or prying action. Additionally, thicker flanges were less susceptible to prying. With the diameter of the bolt increasing from 12 mm to 16 mm, the capacity increased by 21.4%.

Designing the flange bearing resistance against the membrane shear component can increase the T-stub's ductility at extremely large deformation. Finite element calculations estimate the hole's design force as 0.2 times the bolt's tensile resistance. Constructional flaws, such as web misalignment and flange bowing, only affect bolt action. These discrepancies are minimal and can be ignored for the examined flaw [85].

Five beam-to-column joints, made of austenitic stainless steel, were put through cyclic loading tests by Wang et al. [86]. The joints were connected using welded flange and bolted web connections. Cyclic tests were performed on three beam-to-column joints made of duplex stainless steel by Liu and Shi [87] using welded unreinforced flange-welded web connections, while experimental results from five austenitic stainless steel bolted extended end-plate beam-to-column joints were reported by Bu et al. [88]. Furthermore, Yuan et al. [89] performed a battery of cyclic experiments on stainless steel T-stubs and developed a new hysteretic model. The hysteretic performance of stainless steel end-plate beam-to-column joints has not been thoroughly studied, and only five joints of austenitic grade S31608 were tested under cyclic pressure.

Zhao et al. [90] found that grades S385 and S440 specimens were more malleable than S690 specimens causing brittle fracture. Kong and Kim [10] provided the results of finite element simulations, with a particular emphasis on the anticipation of the first-stage hardness and final-stage moment for T-stub joints. To enhance the moment and initial stiffness capability, a novel model was presented, and the connection collapse mechanisms were investigated.

Sun et al. [91] demonstrated the dampening effect of the heat affected zone (HAZ) by applying shear and axial loads to a T-stub joint. As a result, as the dispersion radius of HAZ was extended, and the initial yield resistance of the T-stub represented a linear distance [91].

Using MRFs, Wang et al. [92] studied the operation of the blind-bolt Hollobolt. Initial stiffness, malleability, and strength of the bolted steel connection were all measured in the analysis. Further, by contrasting the flat angle and the shank diameter of the bolt, it was discovered that the flange thickness had a direct bearing on the stiffness or strength of the blind-bolted connections.

The study in this paper presents the structural responses of a DST connection when loaded laterally. Thus, a few parameters were chosen to examine the connection's response modification. When the connection is subjected to seismic loads, a number of factors must be modified, including the behavioral requirements of the bolt and T-stub, the material of the effective section (from steel to SMA), and the geometry of the stiffener. The fundamental goal of this research was to establish the correct DST connection behavior. Accordingly, the proposed damage indexes, failure modes, and behavioral curves were evaluated so that the structural response of a bolted steel connection may be predicted, allowing for a more robust and efficient overall structural system to be designed. The significance of the

study is to assess the performance of DST connections that include stiffeners and shape memory alloys (SMA) because supplementary elements are increasingly employed in steel connections to improve and alter their behavior. The paper concludes by outlining the necessary steps and projected outcomes for improving the DST link.

2. Finite Element Models

The reference FE model consisted of a full-scale T-stub connection, calibrated by the experimental model (Yang et al. [93]). All other comparative models were developed by altering different parameters from the reference model. This connection is composed of the beam, column, double plates, continuity plate, bolts, and T-stub. The height of the column and length of beams is equal to 1 m. The beam has lateral support to avoid unwanted movement, overturning, and out-of-plane connection rotation during cyclic loading. The load is applied to the free end of the beam. In this research, the methodology employed included the stress amplitude and cycle (SAC) loading protocol [94]. This protocol consists of applying a specific level of stress and a specific number of cycles to a material and then evaluating its response. As for the loading phase, cyclic loading was applied to the tip of the beam section, and a static general analysis method was used.

The sections of the beam and column were H406 × 403 × 16 × 24 mm. The T-stub area was defined by beam flanges, column flanges, and prestressed bolts. The distance between bolts and hole arrangements was defined in the experimental models.

The model assumed that the sliding contact between the bolt shank and the bolt hole, the bolt head and the flange, and the bolt head and the rigid plate was finite, allowing for the simulation of massive slip. Normal behavior was assumed to be hard contact, while tangential behavior was simulated using the penalty friction method. In the literature for steel, stainless steel, and aluminum connections [38,92,95–98], the chosen co-efficient of friction was 0.3, which is within the range of 0.2–0.33.

The specification of the model parts is defined in Table 1, in which values of F_u and F_y for bolts, T-stub, beam, and column are presented. F_y and F_u are yield stress and ultimate stress, respectively.

Table 1. Value of F_y and F_u .

Components	F_y (MPa)	F_u (MPa)
Bolt	912.7	976.1
T-stub	399.61	435.85
Beam or column	399.61	435.85

The axisymmetric condition was established for modeling for computational efficiency. A decrease in the quantity of bolts and interactions was modelled for half of the beam-to-column connection. The length of the T-stub section, the stub column, and the midpoint of the beam were all constrained in the X and Z directions to ensure connection symmetry.

Figure 3 demonstrates a meshing overview of the solid elements. The eight-node 3D solid elements and the reduced integral (C3D8R) were used to deliver high precision at minimal computational cost [33,38,92,99]. Several mesh densities were tested, and eventually, a structured mesh was used with variable densities for each region of the model. In order to accurately capture their out-of-plane flexure and prevent the effect of shear locking, at least three elements were given through the thickness of the T-stub. According to [95–97,99], a flange's thickness should have at least two elements across it for bending to be effective. To better simulate the interface between the bolt and the T-stub and to capture contact, a finer mesh was employed around the smaller region of the bolt [99].

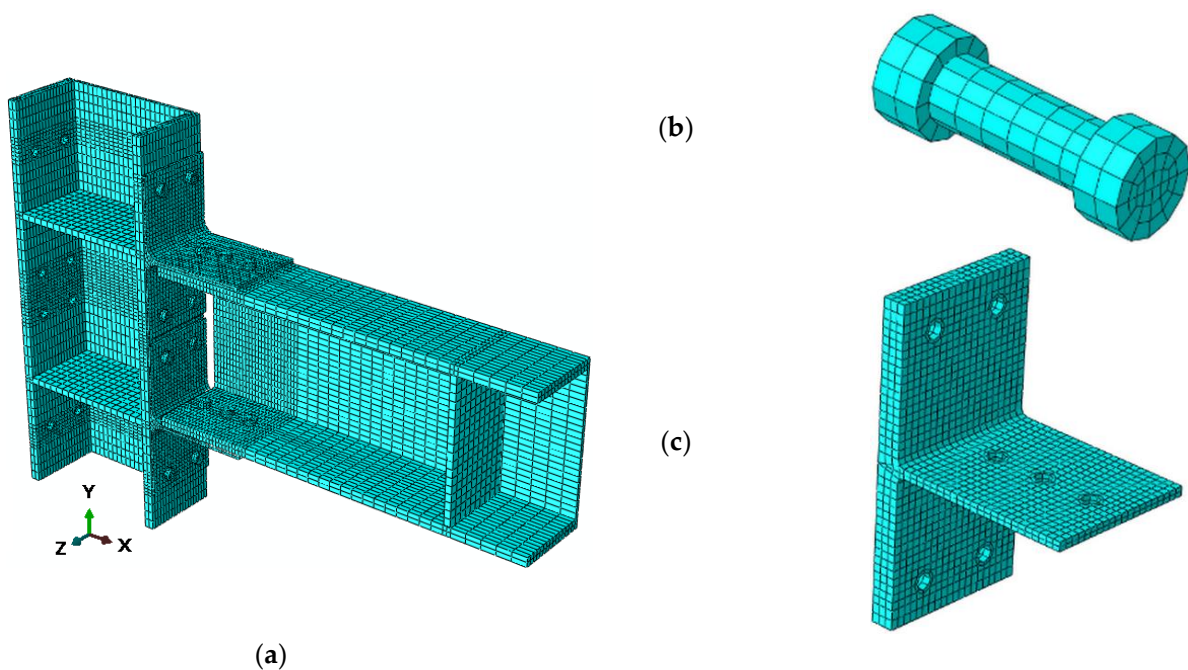


Figure 3. Details of T-stub connection mesh: (a) overview, (b) bolt, and (c) T-stub.

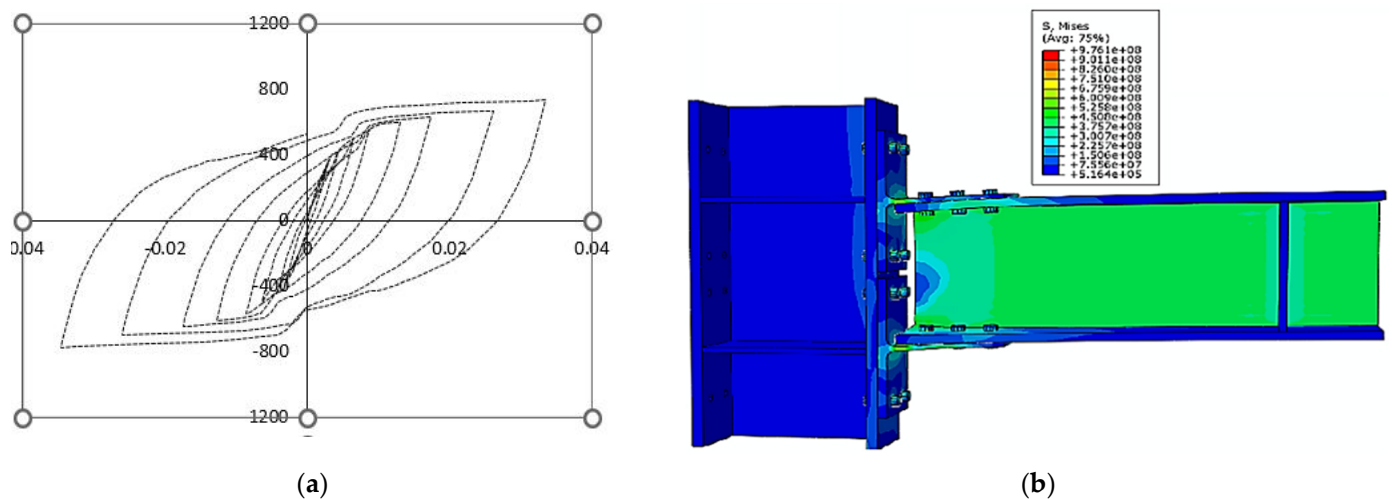
Mesh sensitivity analysis was conducted to obtain an optimized mesh size for all elements of the T-stub connection. Several mesh sizes were studied to determine the size that provided the best accuracy. In the panel zone, which was subject to more stress and strain variations, and also for the T-stub sections and column bolts, which underwent significant yielding, finer meshes were specified.

The total numbers of nodes and elements were 32,760 and 19,572 with linear hexahedral elements (C3D8R), respectively. The column section's mesh sizes at the surroundings of the bolt hole and bolt section were 1.8 and 3.6 cm, respectively. The beam's mesh size adjacent to an area of the column was about 1.5 cm. In addition, plates and T-stubs were supposed to be 2.1 cm and 1.8 cm, respectively. Mesh sensitivity analysis was conducted to compare the stress value of the T-stub section or area as it provided an optimized meshing size.

The analysis had two steps; in the first step, the bolts were prestressed using the bolt load method (AISC 360-16(2016) and RCSC (2014)) [100,101]. In the second step, the cyclic loading was applied to the beam's free end. The numerical modeling results were compared with six specimens experimentally [93], as shown in Table 2. The effective parameters were M_0 , M_{max} , and θ_{max} defining the reference moment of the T-stub, maximum moment, and maximum rotation, respectively. As a result, the maximum error of numerical modeling was approximately 3.47% compared with the experimental results. Figure 4 illustrates the force–displacement curve and Von Mises distribution for the experimental specimen (G310-T19-B400). The stresses concentrated on the T-stub through the beam rotation, and the critical stress and local deformation were revealed in beam flanges and bolts, respectively. Nu and Ex are the abbreviation forms of the numerical and experimental values, respectively.

Table 2. Comparing experimental results with numerical modeling results.

Sample Model	M_0 (KN.m)	θ_{max} (%)	M_{max} (KN.m)	
G260-T15-B350	PS1Ex	257.62	0.087	451.22
	PS1Nu	251.88	0.09	442.48
	Error percent	2.23	3.45	1.937
G310-T15-B400	PS2Ex	197.42	0.098	402.4
	PS2Nu	195.23	0.1	399.61
	Error percent	1.11	2.041	0.69
G260-T19-B350	PS3Ex	411.11	0.037	454.36
	PS3Nu	408.34	0.038	435.85
	Error percent	0.674	2.7	4.07
G310-T19-B400	PS4Ex	329.86	0.13	448.68
	PS4Nu	324.52	0.125	443.17
	Error percent	1.62	3.84	1.23
G260-T21-B350	PS5Ex	458.08	0.023	502.84
	PS5Nu	452.34	0.024	495.51
	Error percent	1.253	4.37	1.46
G310-T21-B400	PS6Ex	411.78	0.0385	447.97
	PS6Nu	407.47	0.04	440.73
	Error percent	1.05	3.9	1.62

**Figure 4.** (a) Hysteresis curve and (b) Von Mises stress distribution for G310-T19-B400 model.

The G310-T19-B400 model was considered the verification model (SP02) for further investigation. The parametric specifications for the developed models are presented in Table 3, where t_f , F_{yt} , and F_{yb} are the T-stub's thickness, the T-stub's yield stress, and the bolt's yield stress, respectively. L1 and L2 are the arrangement of bolt holes on the T-stub web, as depicted in Figure 5. All dimensions are in millimeters.

Table 3. Developed finite element models.

Sample Model	t_f (mm)	F_{yt} (T-Stub) (KN)	Bolt Pretension (KN)	* No (Bolt Beam)	F_{yb} (Bolt) (KN)	L_1 (mm)	L_2 (mm)	Stiffener of T-Stub (mm)	Equipped SMA Material
SP01	19	538.5	165	6	912.7	50	150
SP02	19	538.5	165	6	912.7	100	100
SP03	19	538.5	165	6	912.7	150	50
SP04	19	538.5	165	2	912.7	100	100
SP05	19	538.5	165	4	912.7	100	100
SP06	19	538.5	165	6	950.7	100	100
SP07	19	538.5	165	6	874.7	100	100
SP08	19	620	165	6	912.7	100	100
SP09	19	458	165	6	912.7	100	100
SP10	23	538.5	165	6	912.7	100	100
SP11	15	538.5	165	6	912.7	100	100
SP12	19	538.5	190	6	912.7	100	100
SP13	19	538.5	140	6	912.7	100	100
SP14	19	538.5	165	6	*	100	100	Bolt column
SP15	19	*	165	6	912.7	100	100	T-stub
SP16	19	538.5	165	6	912.7	100	100	3PL169 × 15
SP17	19	538.5	165	6	912.7	100	100	3PL169 × 25
SP18	19	538.5	165	6	912.7	100	100	PL169 × 15
SP19	19	538.5	165	6	912.7	100	100	PL169 × 25

* Defines yield strength of SMA T-stub and bolt as discussed in DesRoches et al. [102].

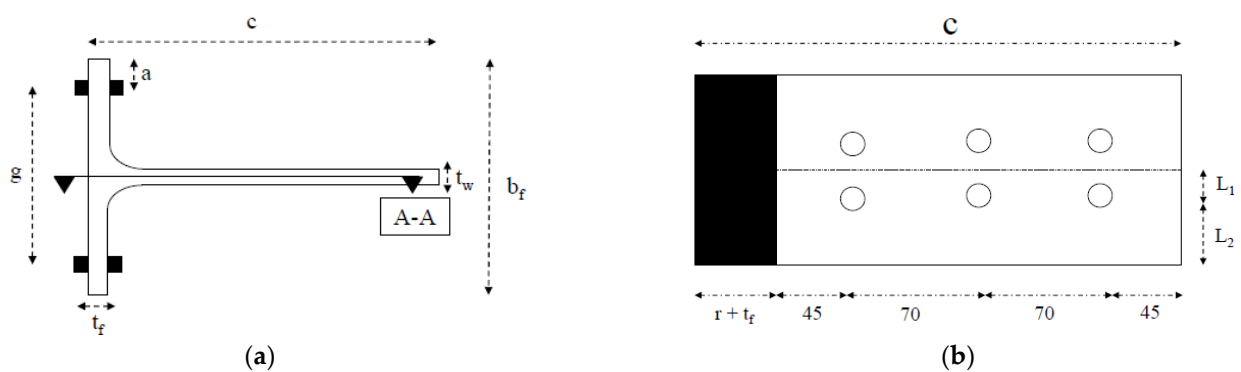


Figure 5. (a) The arrangement of bolt holes on connected T-stub to beam. (b) General schematic of different parameters in T-stub profile.

The SP01 to SP03 models showed a decrease in L_2 value of ~50%. The SP04 to SP07 models were classified based on changing the number and material of bolts. For example, in the SP04 model, the bolts that connected the T-stub section to beam flanges were reduced from six to two in number. Based on the SP08 to SP13 models, a change in the T-stub’s yield stress and thickness or the bolt pretension load could be seen. The steel and SMA were equipped with either a bolt column or a T-stub, as shown in the SP14 and SP15 models. In the SP16 to SP19 models, the T-stub section was equipped with a triangular stiffener as the thickness and number differed.

The Capability of SMA Material

Shape memory alloy (SMA) has been used in seismic applications because it can withstand large loads and recover its original shape by unloading and heating. Utilizing SMA is related to self-centering and energy dissipation capacities in behavior (Wang et al. [103] and Wang and Zhu [104]). According to Pereiro-Barceló et al. [105], the reversible transitions between martensite and austenite identify this distinct property. The SMA likely recovers up to 8% strain in the mode of NiTi alloy because the austenite phase exhibits superplastic behavior (Chowdhury et al. [106]). NiTi material is imported into the ABAQUS based on the mechanical characteristics described in DesRoches et al. [102].

3. Analyzing the Moment–Rotation Curve

The parameters of the moment–rotation curve for 19 models are presented for understanding the behavior of bolted T-stub connection. These parameters include moment capacity, ED capacity, and RD, as shown in Table 4.

Table 4. Moment capacity, ED capacity, and RD.

Specimen	SP01	SP02	SP03	SP04	SP05	SP06	SP07	SP08	SP09	SP10
M_{max} (KN.m)	455.25	450.9	427.82	399.14	447.83	453.94	448.2	455.36	444.46	465.3
ED (KN.m)	142.9	138	110.2	87.96	136.7	139.9	135.9	140.81	135.34	140
RD (mm)	28.65	27.18	25.44	27.58	27	27.23	26.3	27.65	26.81	28.9
Specimen	SP11	SP12	SP13	SP14	SP15	SP16	SP17	SP18	SP19	
M_{max} (KN.m)	440.46	452.56	449.17	417	399.73	541.81	557.5	523.47	545.2	
ED (KN.m)	137	140.9	134.8	142.05	84.75	192.1	213.6	181.8	196.85	
RD(mm)	26.83	28.18	26.58	25.92	18.73	27.38	28.25	26.33	27.84	

A downward trend in the M_{max} , ED, and RD was revealed when there was an increasing trend in the value of L1. For instance, in the SP03 model, ED capacity was reduced compared with the SP02 model (reference model) by about 20%. Similar reductions for the SP06 and SP07 models were observed by a decrease in yield stress of the bolt. A leap in F_{yt} , t_f , or bolt pretension led to enhancing the ED, M_{max} , and RD values. For example, the values of ED, M_{max} , and RD had increments of 1.5%, 3%, and 6%, respectively, where t_f was increased to 23 mm.

A sharp drop in the M_{max} and ED values in the SP15 model could be seen when the T-stub section was equipped with SMA. While an increment trend in the values could be seen when the T-stub was equipped with triangular stiffeners, the maximum ED increased by approximately 55%.

Assessment of Response Curve Variables

The response curve variables are provided by using the force–displacement curve as shown in Figure 6. Table 5 presents the response variable factors. The initial stiffness (K_i) of a bolted steel connection at a drift of 0.3% is defined as the secant stiffness and is calculated from the cyclic response. The residual stiffness or post-yield stiffness (K_r) of a bolted steel connection after the decompression has occurred is also shown, as well as the maximum force (F_{max}) in the connection under lateral loading.

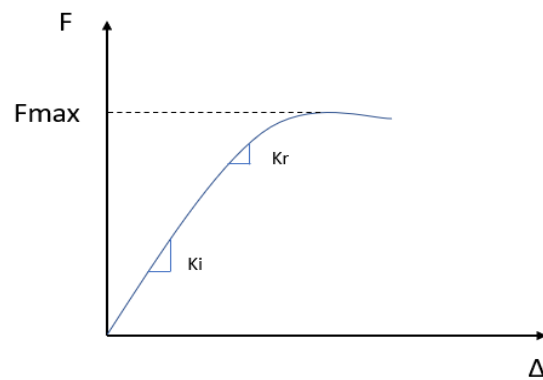


Figure 6. Response variables.

Table 5. Response variables.

Specimen	SP01	SP02	SP03	SP04	SP05	SP06	SP07	SP08	SP09	SP10
Ki (KN.m)	21,709	24,072	24,845	21,148	19,860	19,851	20,354	21,056	19,638	19,758
Kr (KN.m)	10,712	7130	3710	12,476	5918	5720	6729	5994	6410	5980
F _{max} (KN)	737.62	777.43	781.47	688.17	772.12	775.76	774.37	785.11	766.31	776.38
Specimen	SP11	SP12	SP13	SP14	SP15	SP16	SP17	SP18	SP19	
Ki (KN.m)	20,255	20,654	20,062	12,147	17,471	34,440	48,684	29,242	35,300	
Kr (KN.m)	5917	3500	6037	4168	4417	4302	3747	5883	6589	
F _{max} (KN)	776.65	780.27	774.43	719.13	689.2	934.16	961.2	902.54	940	

The values of K_i , K_r , and F_{max} showed a downward trend by the change in F_{yt} and t_f and also when the T-stub or bolt was equipped with SMA material.

The maximum value of K_i limited to the SP17 model was substantially increased by about 102% compared with the SP02 model, while the minimum value showed a 50% decrease for the SP14 model. The value of K_r fluctuated significantly. For example, for the values of the SP12 and SP04 models, the trend decreased by 51% and increased by 75%, respectively. In the SP17 model, F_{max} showed an upward trend of 24%, although its lowest value had a decreasing trend of 11.5% compared with the SP02 model, where the number of beam bolts changed from six to two.

The use of SMA material for the T-stub section resulted in a reduction in the initial stiffness (K_i), residual stiffness or post-yield stiffness (K_r), and maximum force (F_{max}) because of the inherent elastic, resilient, and reversible properties of the SMA material. However, it improved the flexibility and ductility of the DST connection.

As for stiffener-equipped models, these components affected the total response of the connections significantly. The K_i and F_{max} values increased. Stiffeners enhanced the stiffness of the DST connection, and the connection would sustain 5% drift with negligible strength degradation.

Figure 7 depicts the structural behavior curves and Von Mises distributions for models SP14 and SP15. Consequently, in the SP15 model, a reduction in the strength could be noticeably seen compared with the SP14 model. Based on the Von-Mises distribution at a 4% drift, the SP14 model shows a significant focus on stress in comparison to the SP15 model. However, in the SP15 model, there is a sharp increase in the strain energy value that occurs when the drift exceeds 2%.

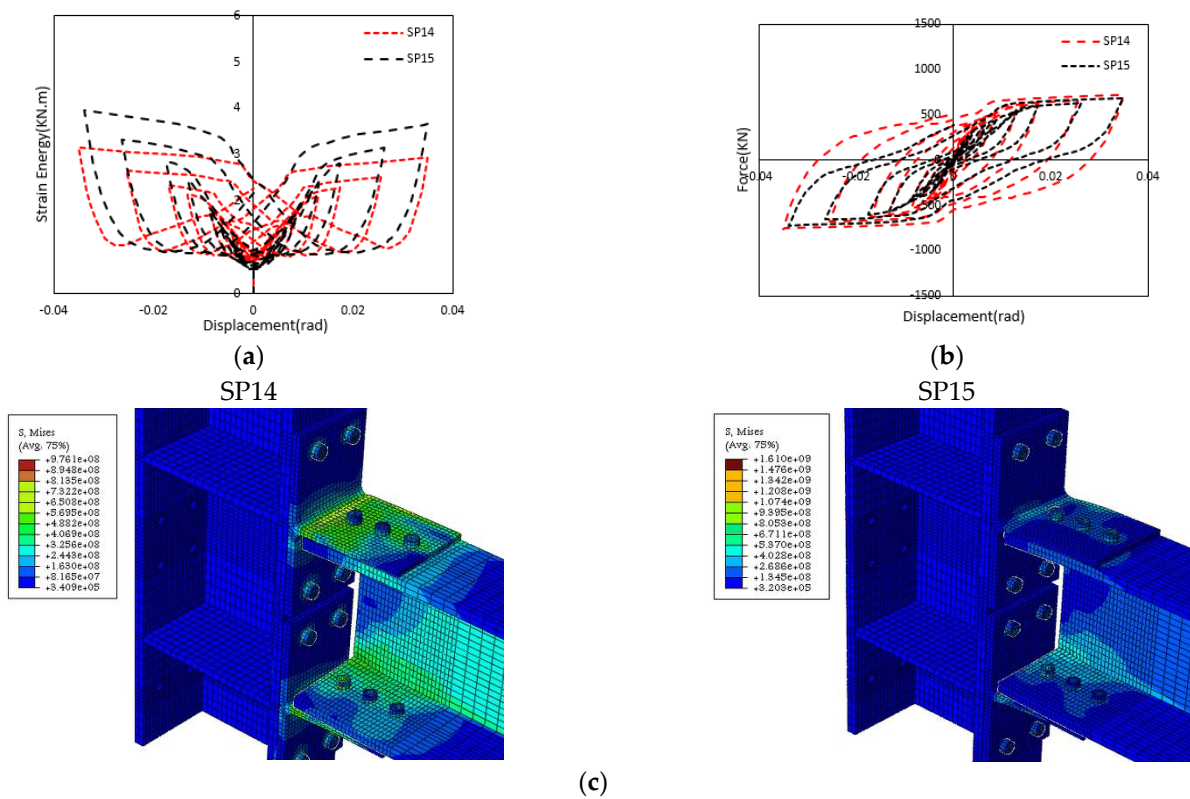


Figure 7. (a) Strain energy-displacement curve. (b). Force- displacement curve (c) Von Mises distribution.

The ductility capacity and residual displacement of the SP14 model were more than 20 and 40%, respectively, compared with the SP15 model. This conclusion was derived from Figure 7b. These changes illustrated more effectiveness of the SMA column bolts than the SMA T-stub in enhancing the ductility and residual displacement of the bolted steel connection.

Figure 8 shows the stress–strain diagram of the SMA T-stub. In this case, the T-stub strain did not exceed 6%. Thus, the conclusion was that the behavior of the SMA materials was simulated correctly.

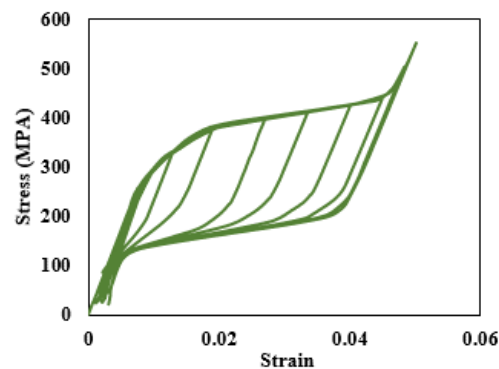


Figure 8. Strain–stress distribution of SMA T-stub under cyclic loading.

4. Failure Indexes

Since fractures or cracks were not explicitly modeled, response indexes could be used to determine the potential level of fracture. There are several commonly used indexes to assess potential fracture, including the pressure index, the Mises index, the triaxiality index (TI), the equivalent plastic strain index (PEEQ), and the rupture index (RI) [107]. An accumulation of high RI values indicated the location of the most potential fracture [108].

Initiating fractures could not be determined by RI. Bozkurt et al. [109–111] recommended using it to compare different configurations to determine the most likely to fracture. In many studies, researchers use the rupture index to evaluate the degree of damage to be experienced at beam-to-column connections [107,112–115].

The T-stub section had a significant role in the DST connection's cyclic behavior to dissipate energy and affect the connection's stiffness and strength.

Equations (1)–(3) show an example of damage index formulations of the T-stub from El-Tawil et al. [116].

$$PEEQ = \sqrt{\frac{2}{3} \varepsilon_{ij}^p \varepsilon_{ij}^p} \quad (1)$$

where the PEEQ index is the ratio of the equivalent plastic strain by the yield strain and ε_{ij}^p is the plastic strain.

$$TI = \frac{PI}{MI} \quad (2)$$

According to Equation (2), the triaxiality index (TI) is the ratio of hydrostatic stress (σ_m) to the Mises stress ($\bar{\sigma}$). The pressure index (PI) is the hydrostatic stress (σ_m) divided by the yield stress (σ_y), and the Mises index (MI) is defined as the ratio of the Mises and yield stress. In Equation (3), the rupture index (RI) is the PEEQ divided by $e^{(1.5 \frac{\sigma_m}{\bar{\sigma}})}$.

$$RI = \frac{PEEQ}{\exp(1.5 \frac{\sigma_m}{\bar{\sigma}})} \quad (3)$$

Additional indexes such as the pressure index, the strain index, and a mix of them were calculated to compare and assess the behavior of the connection system, as shown in Table 6. The stress and strain values were normalized according to the yield stress and strain of the T-stub section.

Table 6. Failure indexes for the developed models.

Sample Model	$\bar{\sigma}$	σ_m	PEEQ	PI	MI	Plasticity Index	TI	RI
SP01	694.2	−567.499	1.09814	−1.0538	1.2891	463.1547	−0.8175	3.7428
SP02	694.2	−497.691	0.511864	−0.9242	1.2891	215.8853	−0.7169	1.5003
SP03	667.68	−470.156	0.341547	−0.8730	1.2399	144.0518	−0.7042	0.9821
SP04	694.2	−419.191	0.241981	−0.7784	1.2891	102.0586	−0.6038	0.5986
SP05	694.2	−468.181	0.566258	−0.8694	1.2891	238.8266	−0.6744	1.5572
SP06	694.2	−497.293	0.511835	−0.9235	1.2891	215.8730	−0.7163	1.4990
SP07	676.48	−484.384	0.508633	−0.8995	1.2561	214.5225	−0.7161	1.4889
SP08	694.2	−509.196	0.470578	−0.9456	1.2891	198.4723	−0.7335	1.4140
SP09	694.2	−488.235	0.544232	−0.9066	1.2891	229.5369	−0.7033	1.5629
SP10	694.2	−499.25	0.51937	−0.9271	1.2891	219.0510	−0.7192	1.5274
SP11	694.2	−493.445	0.492601	−0.9163	1.2891	207.7608	−0.7108	1.4307
SP12	694.2	−498.05	0.527099	−0.9249	1.2891	222.3108	−0.7174	1.5462
SP13	646.8	−469.976	0.486086	−0.8727	1.2011	205.0130	−0.7266	1.4457
SP14	694.2	−494.392	0.472123	−0.9181	1.2891	199.124	−0.7122	1.374
SP15	1309.81	−347.098	0.025471	−0.6445	2.4323	10.7427	−0.265	0.03790
SP16	596.152	−386.19	0.07693	−0.7171	1.1071	32.4463	−0.6478	0.2033
SP17	553.96	−357.88	0.030672	−0.6646	1.0287	12.9363	−0.646	0.0808
SP18	665.99	−433.944	0.170127	−0.8058	1.2367	71.7532	−0.6516	0.4521
SP19	614.55	−420.317	0.101485	−0.7805	1.1412	42.8026	−0.6839	0.2831

The pressure index indicates a failure possibility in the area of the T-stub. The existence of hydrostatic stress in this area increased the likelihood of sudden failure and fracture of the T-stub. Decreasing the number of connected bolts to the beam reduced the T-stub fillet's pressure index and sudden failure possibility. Moreover, a decrease in the spaces between bolts increased the pressure index. It caused improvement in the distribution of ultimate stress and strain on the T-stub section, and finally, the failure of the T-stub section became flexible.

The equivalent plastic strain index (PEEQ) indicates the flexibility of a specific section of the T-stub. The rupture index is the ratio of triaxiality stress (triple ratio). The medium range of triaxiality stress was between values of 0.75 and 1.5 [116]. When the fractural behavior of models became brittle, the triaxiality stress became more than 1.5 or lower than 0.75.

This research compared and evaluated the flange and web area of the T-stub or T-stub fillet index. Increasing the yield stress in the SP08, SP10, and SP12 models changed the value of the rupture index from 1.5 to 1.41, 1.53, and 1.55, respectively. In other words, the fractural behavior of the T-stub became brittle. However, according to the pressure index, increasing the thickness of T-stub and preload of bolts indicated better unexpected fractural behavior in mentioned models.

The rupture index, pressure index, and triaxiality stress index were reduced significantly in models equipped with stiffeners. The reduction of the rupture index of the SP17 model was about 1.05, according to the reference index value (1.5). As a result, the stiffeners improved the sudden fractural behavior of the T-stub section, and the failure of the T-stub connection became flexible.

Failure Modes

This section covers the Eurocode 3 [25] approach. A simple bolted T-stub can fail in accordance with three possible collapse cases, in which the occurrence of a given case typology is governed by the parameter β_{Rd} as shown in Equation (4):

$$\beta_{Rd} = \frac{4M_{f,Rd}}{2B_{Rd}m} \quad (4)$$

In the above equation, $M_{f,Rd}$ is the design flexural resistance of the T-stub flanges, B_{Rd} is the design axial resistance of the single bolt, m is the distance between the bolt axis and the section corresponding to the flange-to-web fillet where the formation of a plastic hinge can be expected, and n is the distance between the bolt axis and the location of the prying force.

In the first case, four plastic hinges were used. Two hinges at the bolt axes assisted with two hinges at the flange to web connection. The value of the design resistance is defined as in Equation (5):

$$F_{1,Rd} = \frac{4M_{f,Rd}}{m} \quad (5)$$

The second case was associated with the formation of two plastic hinges at the sections dealing with the flange-to-web connection and by the fracture of the bolts. The design resistance is given by Equation (6):

$$F_{2,Rd} = \frac{2M_{f,Rd} + 2B_{Rd}n}{m + n} \quad (6)$$

Eventually, the third case was concerned with bolt failure, in which connected plates were fully separated. In this case, the design resistance of the T-stub is given by Equation (7):

$$F_{3,Rd} = 2B_{Rd} \quad (7)$$

To obtain a ductile behavior, the T-stubs must be designed according to mode 1: flange yielding and higher strength should be achieved for the other failure modes, including bolt failure.

Table 7 denotes the failure modes for all 19 models. For instance, the connection did not have any failure modes by equipping the T-stub section or column bolt with SMA material. Mode 3 failure occurred in most developed models. For example, the column bolts failed by an increase in L2 value of about 50%, although mode 2 failure occurred in the SP04 and SP11 models, having different numbers of beam bolts and flange thicknesses of the T-stub section, respectively.

Table 7. Failure modes in developed models.

Specimen	SP01	SP02	SP03	SP04	SP05	SP06	SP07	SP08	SP09	SP10
Failure mode	Mode 3	Mode 3	Mode 3	Mode 2	Mode 3	Mode 3	N/A	Mode 3	Mode 3	Mode 3
Specimen	SP11	SP12	SP13	SP14	SP15	SP16	SP17	SP18	SP19	
Failure mode	Mode 2	Mode 3	N/A	N/A	N/A	Mode 3	Mode 3	Mode 3	Mode 3	

Based on Figure 9, when applying the lateral loads on the SP18 model, mode 3 developed. It showed critical Von Mises stress in the bolt, which illustrated the failure of the bolt. In addition, the behavior of the T-stub flange remained within a limit of the linear region and did not yield.

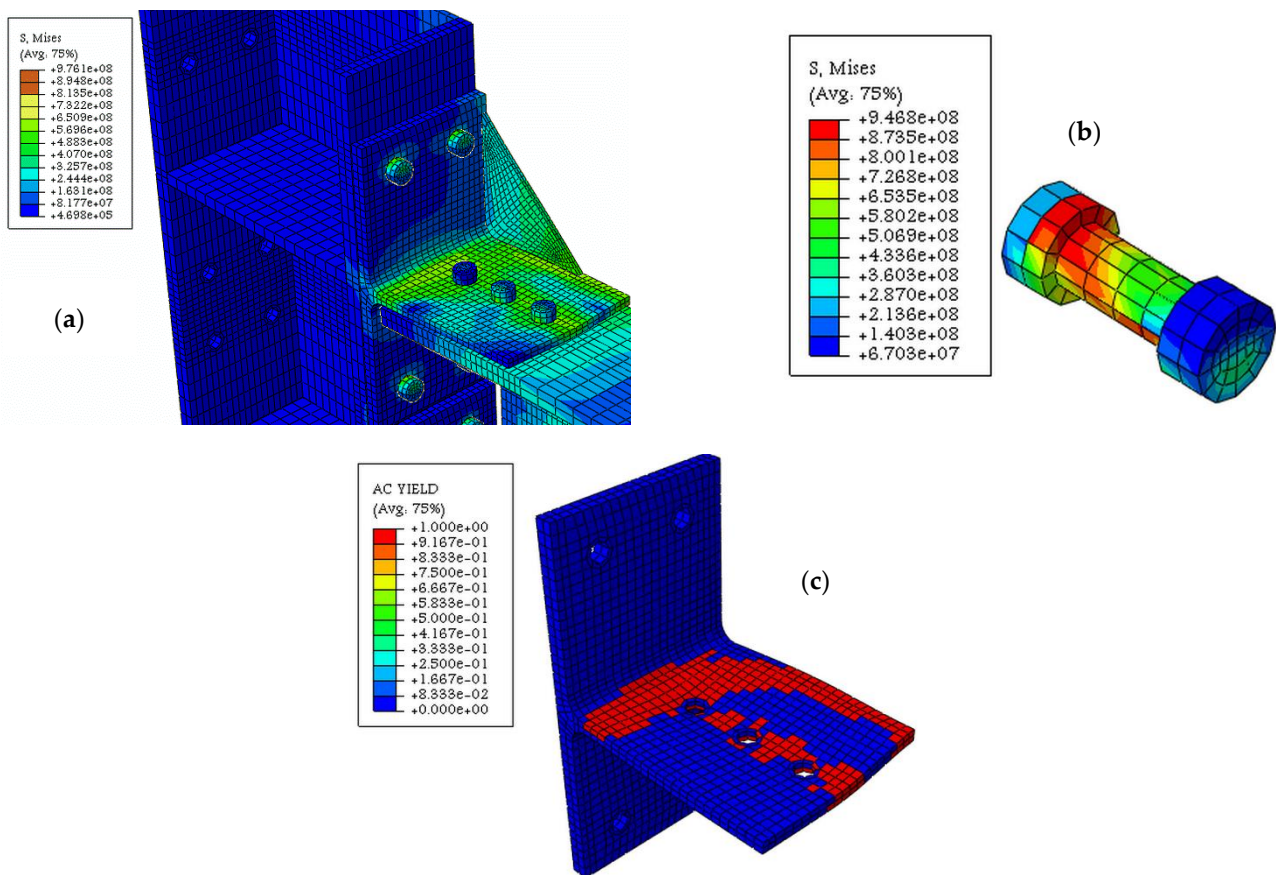


Figure 9. Stress concentration on SP18 model. (a) General view, (b) bolt, and (c) T-stub under cyclic loading.

5. Effects of SMA on Stiffener, T-Stub, and Bolt Column

An SMA material is recognized as an alloy that can be deformed when the temperature drops, while attaining its initial mode shape without residual displacement after increasing the temperature. Such a feature offers intelligent material behavior when subjected to

seismic loads. The effectiveness of the SMA property on the response of models was investigated, in which the T-stubs were equipped with different types of stiffeners.

The newly developed models were named the SP20 to SP43 models, as shown in Table 8. The specifications of the models changed in thickness, number, and type of stiffener and material of components, including the stiffeners, T-stub sections, and column bolts in bolted steel connections. For instance, in the SP28 model, T-stubs were equipped with stiffeners (e.g., type B), and in addition, the material of column bolt was changed from steel to SMA, while as shown in the SP29 model, the T-stubs were equipped with stiffeners (e.g., type A), and the SMA property was assigned to the stiffeners. The stiffeners' dimensions were determined using ABAQUS optimization scripting. Different dimensions were defined in the ABAQUS scripts, and it updated automatically and compared specific results. Figure 10 shows the details.

Table 8. Classification and specification of developed models.

Sample Model	t_f (mm)	No (Bolt Beam)	No (Bolt Column)	L_1 (mm)	Thickness of Stiffener (mm)	Number of Stiffener	Type of Stiffener	Equipped SMA Material
SP20	19	6	4	100	15	3	B	Stiffener
SP21	19	6	4	100	15	3	B	T-stub
SP22	19	6	4	100	15	3	B	Bolt column
SP23	19	6	4	100	15	3	A	Stiffener
SP24	19	6	4	100	15	3	A	T-stub
SP25	19	6	4	100	15	3	A	Bolt column
SP26	19	6	4	100	25	3	B	Stiffener
SP27	19	6	4	100	25	3	B	T-stub
SP28	19	6	4	100	25	3	B	Bolt column
SP29	19	6	4	100	25	3	A	Stiffener
SP30	19	6	4	100	25	3	A	T-stub
SP31	19	6	4	100	25	3	A	Bolt column
SP32	19	6	4	100	15	1	B	Stiffener
SP33	19	6	4	100	15	1	B	T-stub
SP34	19	6	4	100	15	1	B	Bolt column
SP35	19	6	4	100	15	1	A	Stiffener
SP36	19	6	4	100	15	1	A	T-stub
SP37	19	6	4	100	15	1	A	Bolt column
SP38	19	6	4	100	25	1	B	Stiffener
SP39	19	6	4	100	25	1	B	T-stub
SP40	19	6	4	100	25	1	B	Bolt column
SP41	19	6	4	100	25	1	A	Stiffener
SP42	19	6	4	100	25	1	A	T-stub
SP43	19	6	4	100	25	1	A	Bolt column

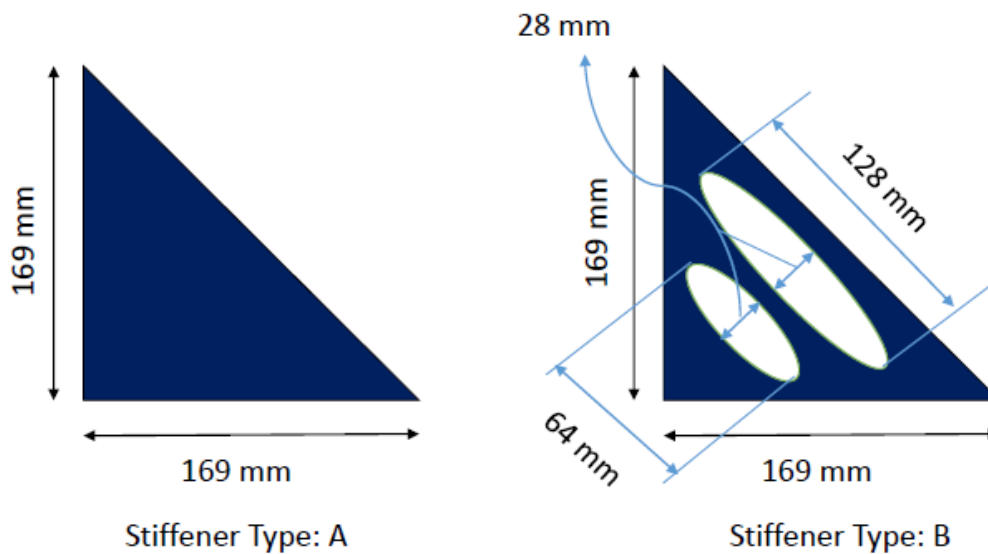


Figure 10. (A,B) Geometric dimensioning of stiffener types.

The stiffeners are reported to have caused rapid growth in the DST connections' initial stiffness and maximum force. Their target in this research was to postpone the early yield and increase the tolerance threshold, which occurred by the enlargement of the initial stiffness of the stiffeners' equipped specimens. Another aim of this section was to modify the stiffeners geometry; there were two types of stiffeners for further investigation.

5.1. Monitoring Behavioural Curve

The force–displacement curves for the SP20 to SP43 models are presented in Figure 11. These curves exhibited the simultaneous effect of the various parameters of importance on the cyclic behavior of bolted steel connection. As a significant result, force values that were enhanced in the models could be observed clearly when comparing with the SP14 and SP15 models for 4% drift. This increasing trend started at approximately 1% drift and was substantially visible between 2% and 4% drifts. In addition, the SP20 to SP43 models indicated a remarkable increase in the residual displacement value compared with the SP15 model. For example, the residual displacement value of the SP30 model increased by 63% when compared with the SP15 model.

As stated in Table 9, an SMA material had beneficial effects on the total performance of DST connections. For example, all three studied parameters (K_i , K_r , and F_{max}) for SP26 were higher than those of SP02. This validated the usage of stiffeners, either steel or SMA materials. It consistently increased the initial stiffness (K_i) and ultimate strength (F_{max}) of the connection (each by 113.52% and 15%), while the first yield point of the connection was delayed (higher post-yield or residual stiffness).

Table 9. The parameters of the response curve.

Specimen	SP20	SP21	SP22	SP23	SP24	SP25	SP26	SP27	SP28	SP29	SP30	SP31
K_i (KN.m)	52,452	40,758	40,550	53,813	50,839	46,142	51,400	49,365	43417	637,812	62,677	33,782
K_r (KN.m)	6024.2	4966.7	6976.2	2995.2	2860	5901.1	6049	2787.5	6061.4	2888.4	2964.7	6884.8
F_{max} (KN)	903.91	859.88	893.02	905.02	873.7	884.59	898.64	874	898.98	936.24	927.67	933.52
Specimen	SP32	SP33	SP34	SP35	SP36	SP37	SP38	SP39	SP40	SP41	SP42	SP43
K_i (KN.m)	48,168	45,036	39,201	48,720	43,267	41,326	49,444	44,392	39,722	55,153	55,666	48,044
K_r (KN.m)	2613.2	3571	2794.3	3436.8	3510.3	2870	2998.6	3402	3082.3	2572	2989.2	2778.7
F_{max} (KN)	875.46	826.82	850.24	869.38	830.87	856.18	875.46	824.27	854.91	912.73	880.57	916.7

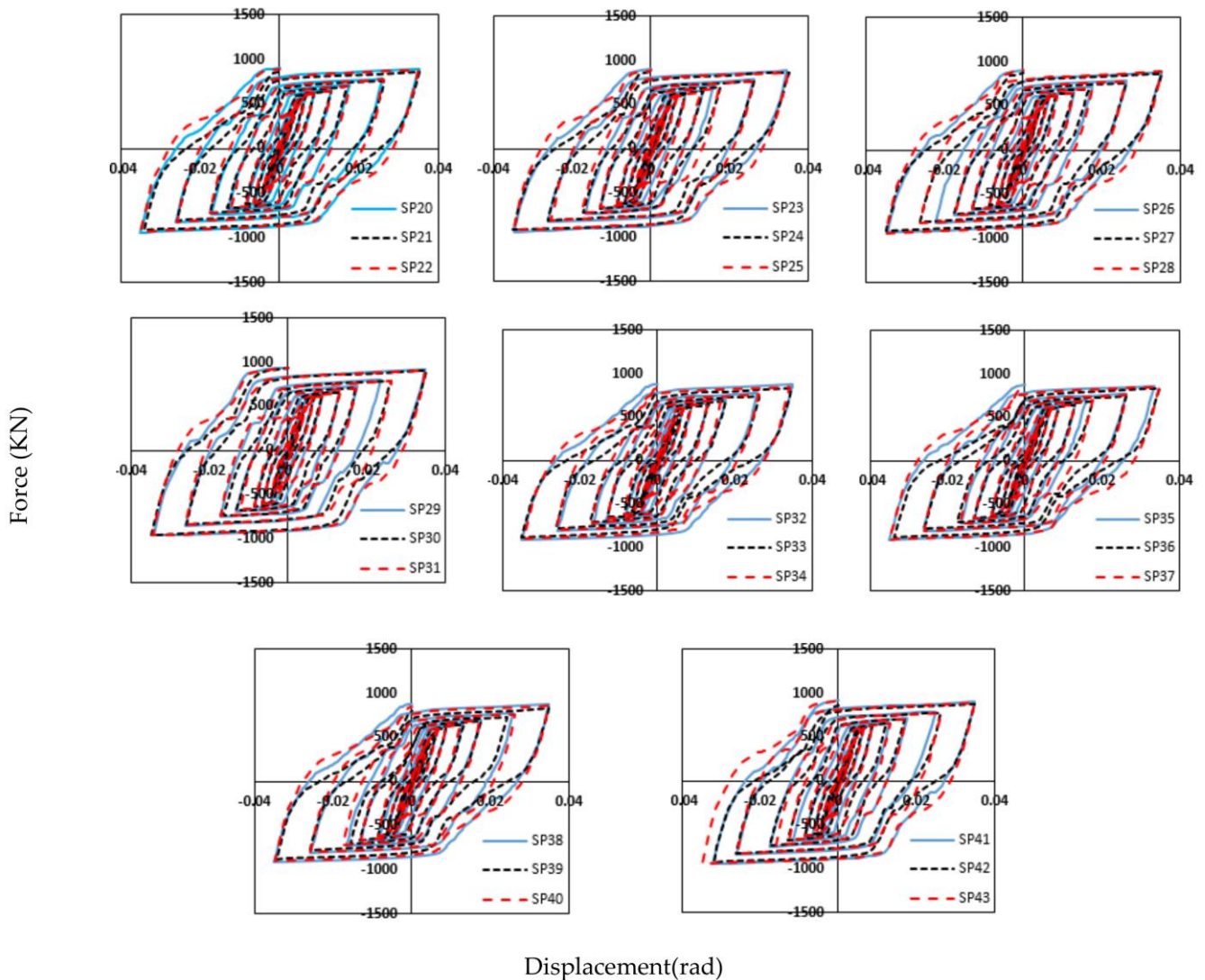


Figure 11. Force–displacement curves.

Another vital element alongside the stiffener was the T-stub section. The overall performance and response of the DST connections depended on the deformation quality and status of the T-stub section. SP15 was an example where it had an SMA type T-stub section, in which the initial slope of the force–displacement curve (K_i) and F_{max} experienced a percentage decrease of 27.4% and 11.8%. This reduction showed that SP15 was more flexible and ductile when compared with the original specimen (SP02), whereas the T-stub section could rebound or return to its preliminary position due to the inherent SMA material specifications. These results conclusively supported the reasons for using SMA material.

As shown in Figure 12, for the DST connection, the existence of the SMA column bolt and changes in the number and thickness of the stiffener increased the value of M_{max} when compared with SP14, from 19% to 30%. Equipping the connection with the SMA T-stub section and changing the number and thickness of stiffeners led to changes in the M_{max} value. This increase was between 19.6% to 34.6% when compared with the SP15 model. As shown in Figure 13, for non-reference models where the column bolt or T-stub section was equipped with SMA property, a change was seen in the number or thickness of the stiffeners simultaneously. The ED capacity of the SP24 and SP25 models increased when compared with the SP14 and SP15 models.

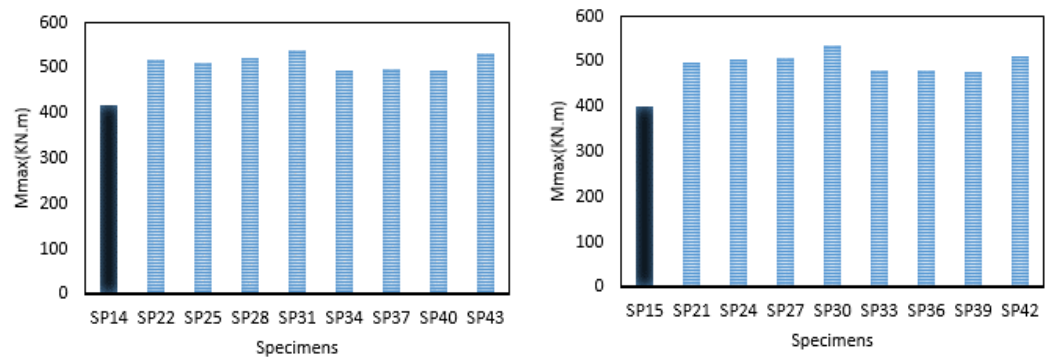


Figure 12. M_{max} of all connections.

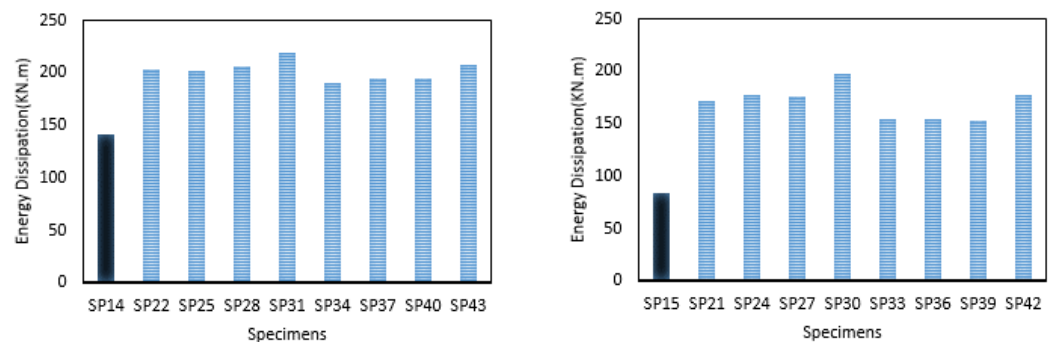


Figure 13. ED capacity of all connections.

5.2. Equivalent Viscous Damping Ratio

As for further investigation of the connection behavior and response, another index was introduced to show the dissipation potential of the DST connections, exclusively in the specimens equipped with T-stub stiffeners. This index was called the equivalent viscous damping ratio (EVDR), a dimensionless index that could be calculated by Equation (8) [117–119]:

$$\xi = \frac{E_D}{4\pi E_{S_0}} \quad (8)$$

where ED is the total energy loss per loading cycle and Es is the strain energy in an elastic system with identical maximum deformation and force to a nonlinear system.

Considering Figure 14, Ed and Es are the total energy loss per loading cycle and strain energy in an elastic system with identical maximum deformation and force, respectively. It is clear that Ed for each specimen would increase by drift increment. The findings in this paper provide additional information about the definition of the equivalent viscous damping ratio and its usage in assessing steel or composite connection [117,118,120–122].

According to the EVDR/drift figures, the application of stiffeners affected the energy dissipation of the DST connections; EVDR increased up to 20% in a 4% drift. That showed a successful modified and developed edition of an original specimen (a stiffener-free model). Figure 15 shows the subsequent results on the EVDR versus drift level for all stiffened specimens.

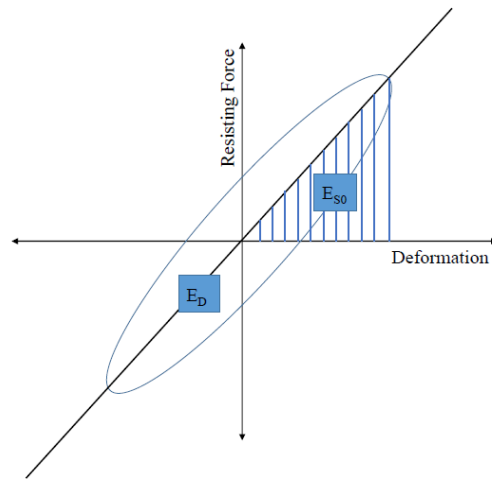


Figure 14. Illustration of total energy dissipation E_D and maximum strain energy E_{S0} [119].

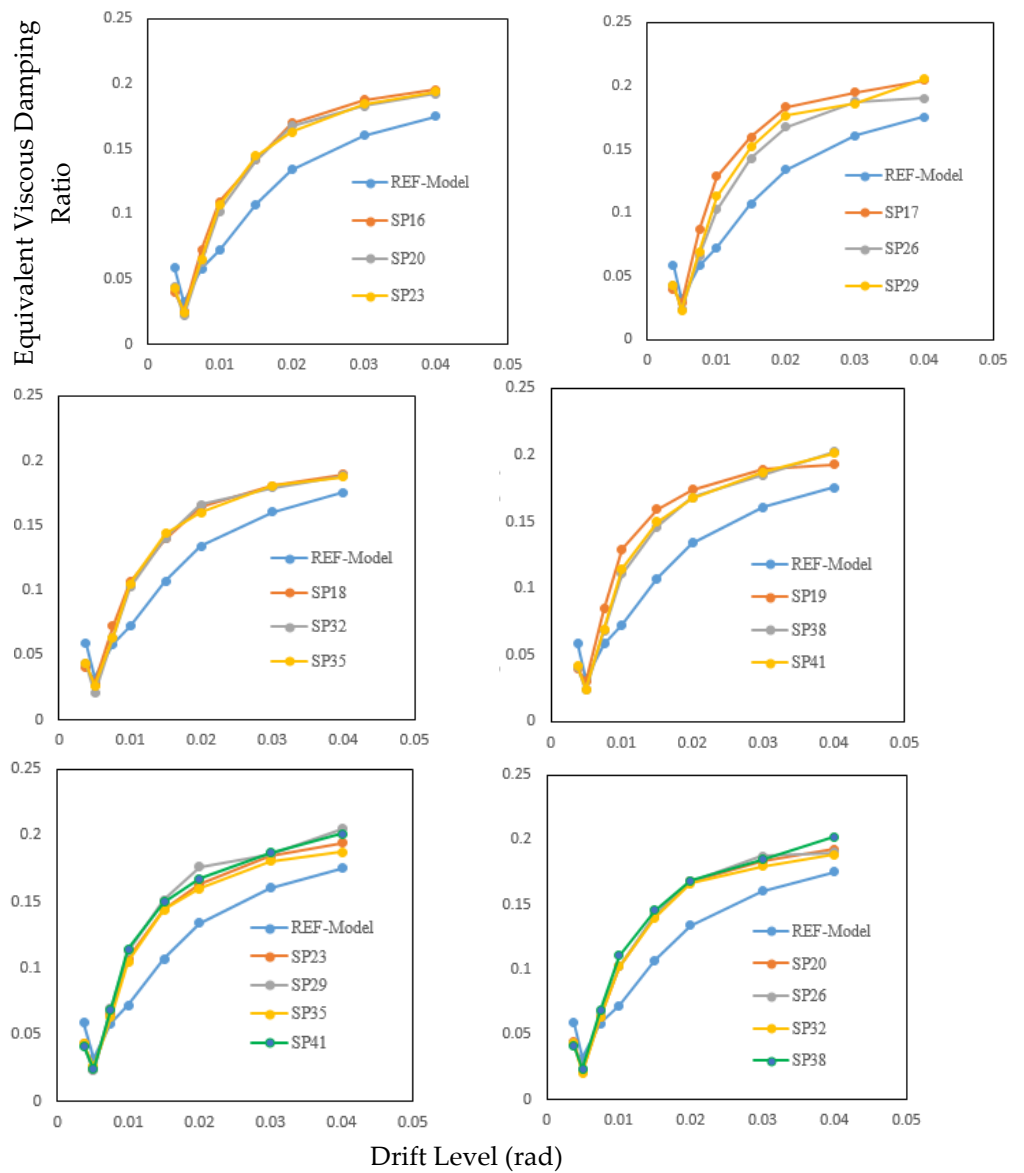


Figure 15. EVDR versus drift level.

5.2.1. Ductility Capacity and Failure Modes

Ductility is the ability to endure the nonlinear deformations without failing. Using this concept in analysis and design can guarantee the optimized performance of a structure, when facing strong lateral displacements. The ductility ratios of the models were calculated by the equivalent energy elastic–plastic (EEEP) method that has been recommended by ASTM E2126-11 [123]. The ductility ratio is defined as the ratio of the ultimate displacement to the yield displacement (rotation), respectively, and is shown in Equation (9).

$$\mu = \frac{\Delta_u}{\Delta_y} \tag{9}$$

The connection behavior had a straight/linear relationship with the value of the ductility ratio. The equivalent energy elastic–plastic method used two enclosed areas by intersecting three points on the curve: namely, yield, maximum, and ultimate point. Figure 16 shows that A1 and A2 were created with intersection of the curve lines with equal areas.

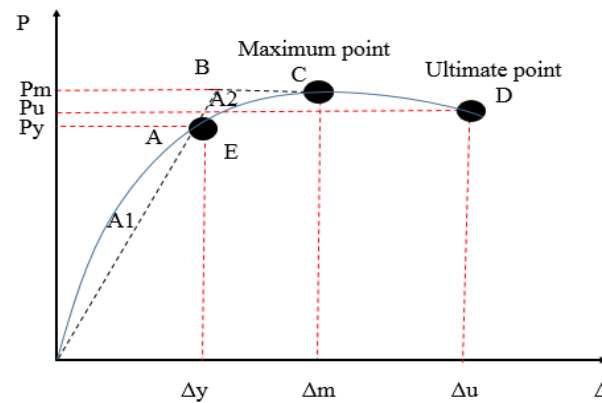


Figure 16. Equivalent energy elastic–plastic (EEEP) method.

As shown in Table 10, the extents of ductility revealed fluctuations from 2.66 to 3.97. The maximum and minimum values were calculated for the SP29 and SP39 models, respectively.

Table 10. Ductility and failure modes.

Specimen	SP20	SP21	SP22	SP23	SP24	SP25	SP26	SP27	SP28	SP29	SP30	SP31
θ_y (rad)	0.012	0.013	0.012	0.011	0.013	0.011	0.013	0.012	0.01	0.013	0.011	0.011
θ_u (rad)	0.0349	0.0349	0.0348	0.0345	0.0349	0.0344	0.0349	0.0349	0.0349	0.0348	0.0349	0.0349
M_y (KN.m)	385.92	373.61	382.11	385.37	376.4	376.19	382.45	375.51	384.48	399.42	392.52	395.94
$\mu = \frac{\theta_u}{\theta_y}$	2.99	2.68	2.88	3.11	2.67	3.17	2.68	2.78	3.33	2.66	3.04	3.24
Failure mode	3	3	N/A									
Specimen	SP32	SP33	SP34	SP35	SP36	SP37	SP38	SP39	SP40	SP41	SP42	SP43
θ_y (rad)	0.01	0.01	0.012	0.01	0.009	0.013	0.011	0.008	0.012	0.011	0.009	0.012
θ_u (rad)	0.0348	0.0345	0.0341	0.0334	0.0347	0.0347	0.0348	0.0347	0.0346	0.0348	0.0347	0.0346
M_y (KN.m)	377.55	359.25	369.42	375.06	361.01	372	377.55	358.14	371.45	391.08	382.6	387
$\mu = \frac{\theta_u}{\theta_y}$	3.32	3.84	2.81	3.25	3.61	2.68	3.11	3.97	2.85	3.07	3.82	2.74
Failure mode	3	3	N/A									

The results could be observed that an increase in the stiffener thickness reduced the ductility ratio only when the stiffener type was equipped with SMA material. For example, in the SP26 model, there was 11% reduction in the ratio in comparison with the SP20 model. Simultaneously, having an SMA T-stub or SMA column bolt increased the ductility ratio. As for the SP33 and SP39 models, the effectiveness of the SMA T-stub and stiffener thickness in the ductility ratio was observed.

Regarding the effect of the number of stiffeners, the ductility ratio in the SP43 model was compared with SP31. The existence of the SMA column bolt and change of stiffener number from one to three resulted in an 18% increase. However, the exact change in the number of stiffeners and of the addition of the SMA T-stub or SMA stiffener in the bolted steel connection led to reducing the ductility ratio.

Table 10 also illustrates the failure modes for the SP20 to SP43 models. It was shown that mode 3 occurred in the models having stiffeners or T-stub with SMA properties. Figure 17 shows a representative mode 3 failure for SP32. The Von Mises distribution in the bolt was evaluated critically, and the bolt failed. However, the distribution of the AC yield in the T-stub revealed that the flange of the T-stub did not yield. The models that included the column bolt with SMA properties did not experience any failure.

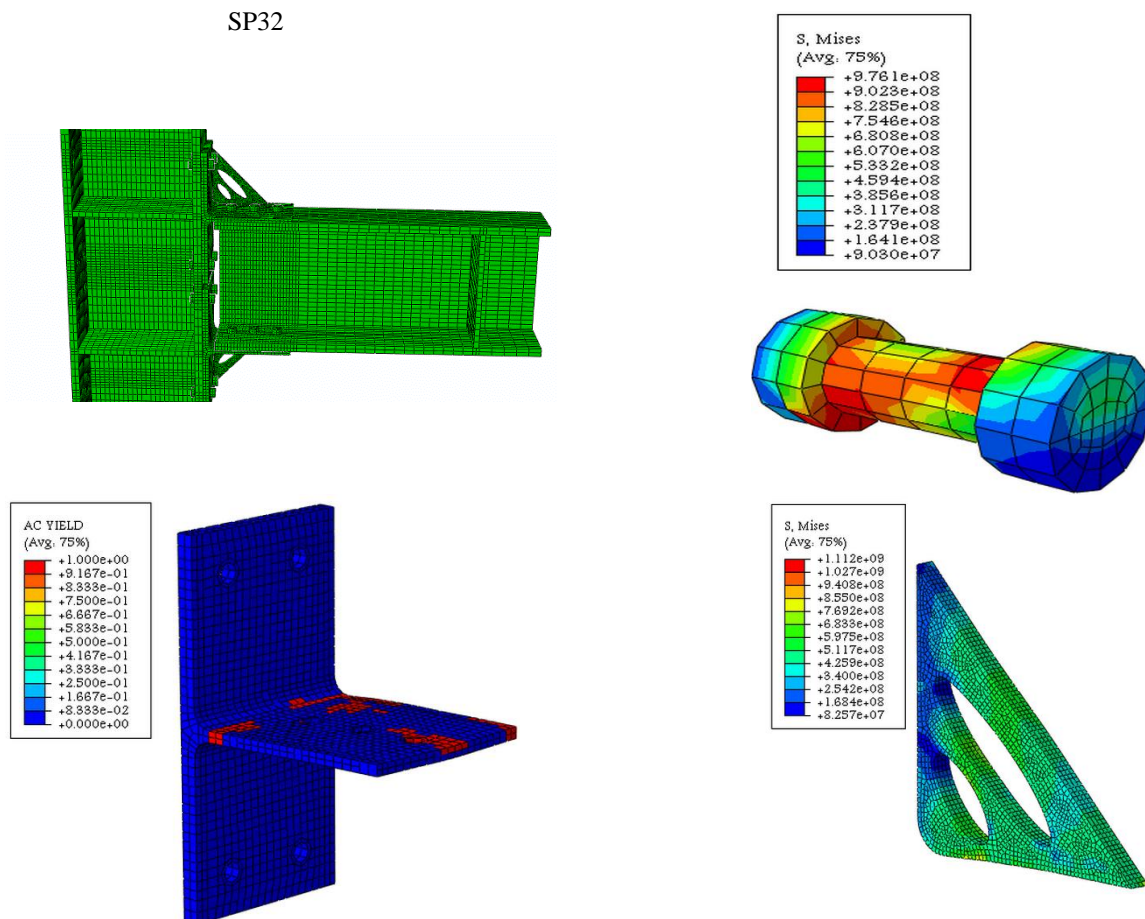


Figure 17. Distribution of Von Mises and AC yield (MPa) for the SP32 model.

5.2.2. Bolt Force, Strain Energy, and Frictional Energy

Figure 18 illustrates the frictional dissipation capacity for 12 specimens that were subjected to cyclic loading. The capacity of the models for bolts having SMA was compared with other models in which the T-stub material or stiffener material was changed from steel to SMA. For example, at the end of lateral loading, the frictional dissipation of the SP28

model was about 28 KN.m. However, the dissipation of models such as SP26 and SP27 was limited to approximately 12.5 KN.m.

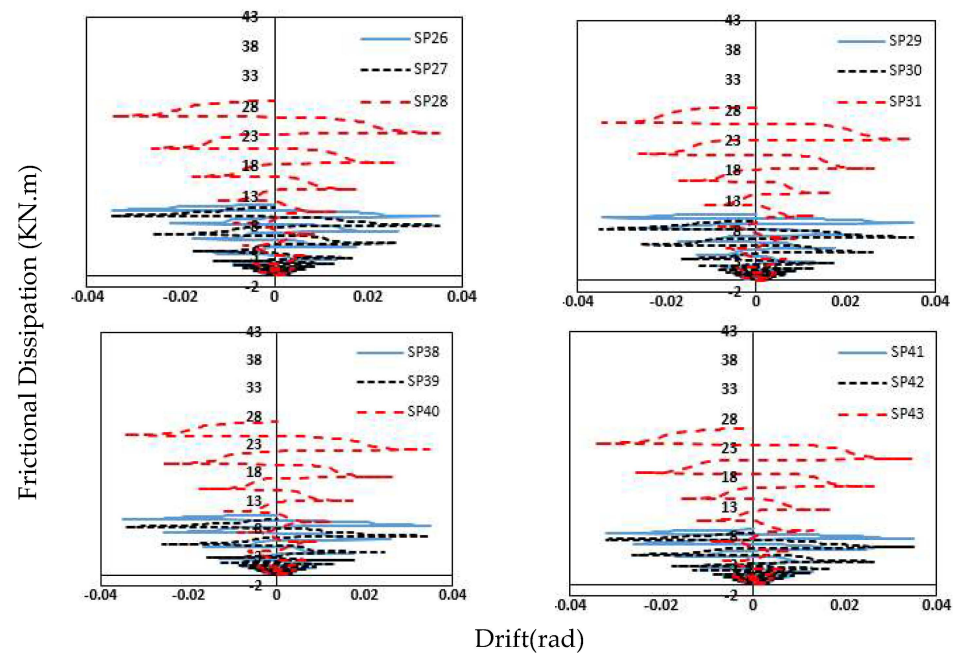


Figure 18. Frictional dissipation and drift.

Based on the dissipations, the simultaneous change in the number of stiffeners and the material of the stiffeners, bolts, or T-stubs did not significantly affect the frictional dissipation in the bolted steel connection.

The strain energy was obtained from the strain and stress created in the part or body and the volume change of the body undergoing deformations. The strain energy was generated in the elastic phase of the part so that the body sustained some stress due to loading and underwent local deformation and strain. Total deformation led to altering the volume and structure of the part. The strain energy was directly related to the part's volume variation rate.

The total strain energy consisted of two elastic and non-elastic (plastic) phases. Thus, the figures show that the connection remained elastic in the drifts below 1%, and the elastic strain energy was formed. However, when the rotation increased from 1% to 4%, the connection tolerated plastic deformations due to increased stresses on the connecting parts.

As discussed before, the reason for the lower total energy dissipation and strain energy of SP27 (176.3 KN.m) was type B stiffeners. Since this type of stiffener had drilled holes, the volume of the part was less than the other stiffener type (without drilled holes or the solid one); hence, higher strain energy is observed from SP30 (197.9 KN.m). The reason for the proposed type B stiffener was its high capacity for total energy dissipation. The induced deformation and stress in the stiffener increased with increasing loading intensity, and this enhancement resulted in the loss of connection internal energy through significant plastic strains as shown in Figure 19.

As shown in Figure 20, at the beginning of loading, the force generated in the bolts of all three models was approximately identical. If the loading intensity or the step time increased, the difference between the generated forces of the bolts was insignificant.

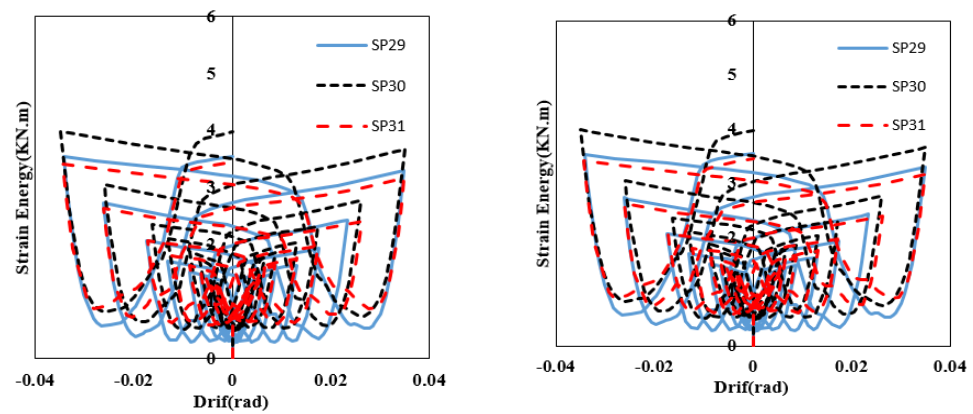


Figure 19. Strain energy and drift.

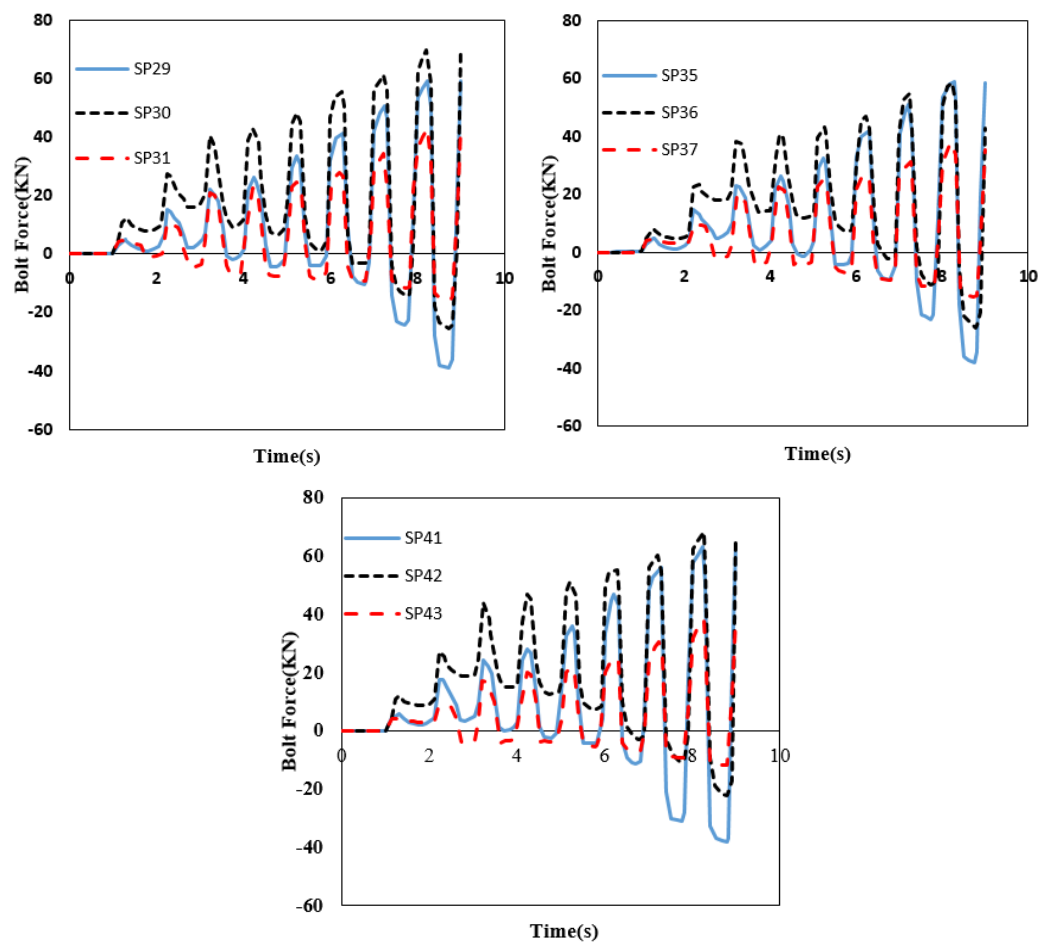


Figure 20. Bolt force and time.

In other words, an increment in the bolt force was due to the increase in the connection rotation. At drifts above 3 to 4%, the bolts underwent high tensile stress, and the bolts could be brought to the yield point threshold and could eventually collapse and rupture.

Among three models, the maximum bolt force was observed for SP30, with SMA T-stub (double split tee section). Such an improvement in the bolt force was due to a large amount of plastic deformation in the T section because of high drifts and with respect to the SMA alloy properties. The T-stub sought to restore all deformations and strains created in the preloading state or its initial state by adding large tensile forces to the bolts. The beam rotation caused the T-stub flange to rotate, and the bolts connected to the column flange prevented that rotation. Therefore, the forces in bolts were increased sharply for each cycle.

Ultimately, the addition of the stiffeners had a considerable influence on the behavior and performance of T-stub connections, ultimate moments, and energy dissipation capacity. The ultimate moment was responsible for decaying the internal energy in the connection and reducing the amount of damage induced. The change allowed for the optimization of the proposed connection, which increased the energy dissipation capacity of the T-stub and resulted in material savings for manufacturing stiffeners. Therefore, the use of type B stiffeners caused more energy loss, and the connection withstood more bending moments before failure.

6. Conclusions

This paper presented the cyclic performance and response of double split tee connections, specifically quantifying the addition of stiffeners. The findings revealed that reducing the number of bolts used in the beam caused a decrease in the connection's ultimate moment by up to 11%. Increasing the thickness of the T-stub, the yield stress of the T-stub and bolts, and the bolt preloads, however, improved the connection's moment capacity. Adding a column bolt to the SMA decreased the connection's ultimate moment due to the SMA's behavior and the high stress levels of austenite and martensite. Additionally, including triangular stiffeners in the models increased the connection's stiffness, resulting in an increase in the ultimate moment and moment capacity of the models with 15 mm and 25 mm thickness stiffeners by 16% and 21% times compared with the reference models.

The research found that increasing the number of bolts and the yield stress of the T-stub led to an increase in the failure index and a sudden brittle fracture. However, models with a higher T-stub thickness and bolt preload showed an increased failure index. This indicated that the haunch of the T-stub was more likely to experience a high brittle fracture at a 4% drift. The use of stiffeners on the T-stub improved the performance of the DST connection by decreasing the failure index, pressure index, and triaxiality index. Specifically, the failure index was reduced by 69% when using a 15 mm thick stiffener. The stiffeners improved the behavior of the T-stub and reduced its likelihood of failure, making their use in bolted steel connections recommended. Additionally, using an SMA T-stub in the DST connection improved its role as an energy dissipater and the overall performance of the connection.

The study found that the failure mode of the models was mode 1 when the T-stub, bolts, or stiffeners were made of SMA materials. However, when changes in the bolt pretension, the yield stress of the T-stub, or the thickness of the T-stub were made, the failure mode switched to mode 2. Additionally, reducing the number of bolts from six to four or two led to a switch in failure mode from mode 1 to mode 3.

In terms of the energy dissipation capacity, increasing the number of bolts and the thickness and yield stress of the T-stub increased the ED capacity of the beam. The models with SMA material also showed an increase in energy dissipation. On the other hand, using stiffeners on the T-stub also increased the ED capacity, with those using three stiffeners with 2.5 cm thickness showing a 55% improvement in ED capacity.

Additionally, the study found that the K_i value of connections reinforced by steel and SMA stiffeners was greater than that of the reference model. The K_r variable was, however, reduced by 58% when using an SMA stiffener. The equivalent viscous damping ratio (EVDR) was also increased for the modified and stiffened models with steel and SMA stiffeners when compared with the reference model.

In comparison with the stiffener-free specimens, the specimens with steel/SMA stiffeners exhibited higher income energy, primarily due to inelastic/plastic deformation. Despite slight differences, the DST connections with steel/SMA stiffeners demonstrated increased ED capacities, K_i , K_r , and F_{max} when compared with the reference model.

Recommendations for further studies include the following:

- Investigating the use of different types and thicknesses of stiffeners to determine their impacts on the connection's performance.

- Examining the effects of different T-stub thickness, yield strength, and bolt preload to improve the ultimate moment and ED capacity of the connection.
- Evaluating the behavior and performance of the connection with different types of loading conditions, such as cyclic, static, and dynamic loading.
- Conducting more comprehensive tests, such as shake table testing, to evaluate the real-world performance of the connection in seismic situations.
- Performing a detailed cost–benefit analysis of using different materials and designs to optimize the practicality and cost-effectiveness of the connection.
- Investigating the behavior of the DST connection under different loading conditions such as cyclic loading, static loading, and dynamic loading.

Author Contributions: Conceptualization, A.T. and N.A.; methodology, H.H.; software, N.A. and A.T.; validation, H.H., A.T. and N.A.; formal analysis, G.U.; investigation, N.A.; resources, S.Y.; data curation, A.T.; writing—original draft preparation, N.A.; writing—review and editing, G.U.; visualization, A.T. and S.Y.; supervision, G.U.; project administration, H.H. All authors have read and agreed to the published version of the manuscript.

Funding: This research received no external funding.

Data Availability Statement: Data sharing is not applicable to this article. Data is unavailable due to privacy or ethical restrictions.

Conflicts of Interest: The authors declare no conflict of interest.

References

1. Grecea, D.; Dinu, F.; Dubină, D. Performance criteria for MR steel frames in seismic zones. *J. Constr. Steel Res.* **2004**, *60*, 739–749. [[CrossRef](#)]
2. Carter, C.J.; Iwankiw, N.R. Improved ductility in seismic steel moment frames with dogbone connections. *J. Constr. Steel Res.* **1998**, *46*, 448. [[CrossRef](#)]
3. Engelhardt, M.; Winneberger, T.; Zekany, A.; Potyraj, T. Experimental Investigation of Dogbone Moment Connections. *Eng. J.* **1998**, *35*, 128–139.
4. Montuori, R.; Nastri, E.; Piluso, V.; Troisi, M. Influence of connection typology on seismic response of MR-Frames with and without ‘set-backs’. *Earthq. Eng. Struct. Dyn.* **2017**, *46*, 5–25. [[CrossRef](#)]
5. Montuori, R.; Nastri, E.; Piluso, V. Advances in theory of plastic mechanism control: Closed form solution for MR-Frames. *Earthq. Eng. Struct. Dyn.* **2015**, *44*, 1035–1054. [[CrossRef](#)]
6. Faella, C.; Montuori, R.; Piluso, V.; Rizzano, G. Failure mode control: Economy of semi-rigid frames. In Proceedings of the XI European Conference on Earthquake Engineering, Paris, France, 6–11 September 1998.
7. Tenchini, A.; D’Aniello, M.; Rebelo, C.; Landolfo, R.; da Silva, L.S.; Lima, L. Seismic performance of dual-steel moment resisting frames. *J. Constr. Steel Res.* **2014**, *101*, 437–454. [[CrossRef](#)]
8. Cassiano, D.; D’Aniello, M.; Rebelo, C.; Landolfo, R.; da Silva, L.S. Influence of seismic design rules on the robustness of steel moment resisting frames. *Steel Compos. Struct.* **2016**, *21*, 479–500. [[CrossRef](#)]
9. Paella, C.; Piluso, V.; Rizzano, G. *Structural Steel Semirigid Connections: Theory, Design, and Software*; CRC Press: Boca Raton, FL, USA, 2000.
10. Kong, Z.; Kim, S.-E. Numerical estimation for initial stiffness and ultimate moment of T-stub connections. *J. Constr. Steel Res.* **2018**, *141*, 118–131. [[CrossRef](#)]
11. Guo, H.; Liang, G.; Li, Y.; Liu, Y. Q690 high strength steel T-stub tensile behavior: Experimental research and theoretical analysis. *J. Constr. Steel Res.* **2017**, *139*, 473–483. [[CrossRef](#)]
12. Liang, G.; Guo, H.; Liu, Y.; Li, Y. Q690 high strength steel T-stub tensile behavior: Experimental and numerical analysis. *Thin-Walled Struct.* **2018**, *122*, 554–571. [[CrossRef](#)]
13. Atasoy, M. Determination of Prying Load on Bolted Connections. Master’s Thesis, Middle East Technical University, Ankara, Türkiye, 2012.
14. Kulak, G.; Fisher, J.; Struik, J. *Guide to Design Criteria for Bolted and Riveted Joints*, 2nd ed.; American Institute of Steel Construction: Chicago, IL, USA, 2001.
15. Bezerra, L.M.; Bonilla, J.; Freitas, C.S.; Massicotte, B. Behavior of T-stub steel connections bolted to rigid bases. *J. Constr. Steel Res.* **2022**, *192*, 107242. [[CrossRef](#)]
16. American Institute of Steel Construction. *Steel Construction Manual*, 14th ed.; American Institute of Steel Construction: Chicago, IL, USA, 1927.
17. Douty, R.; McGuire, W. High strength bolted moment connections. *J. Struct. Div.* **1965**, *91*, 101–128. [[CrossRef](#)]
18. Nair, R.; Birkemoe, P.; Munse, W. High strength bolts subject to tension and prying. *J. Struct. Div.* **1974**, *100*, 351–372. [[CrossRef](#)]

19. Zhu, X.; Wu, Z. Study on New Bolted T-Stub Connection with Inserted Plates under Axial and Cyclic Loads. *Appl. Sci.* **2020**, *10*, 2631. [[CrossRef](#)]
20. ABNT NBR 8800; Design of Steel and Composite Structures for Buildings. ABNT: Rio de Janeiro, Brazil, 2008.
21. Struik, J.; de Back, J. *Tests on Bolted T-Stubs with Respect to a Bolted Beam-to-Column Connections*; Stevin Laboratory, Delft University of Technology: Delft, The Netherlands, 1969; pp. 6–69.
22. American Institute of Steel Construction. *Load and Resistance Factor Design (LRFD) Specifications for Structural Steel Buildings*; American Institute of Steel Construction: Chicago, IL, USA, 1986.
23. American Society of Civil Engineers. *Plastic Design in Steel: A Guide and Commentary*; Manual and Report of Engineering Practice Ser. No. 41; American Society of Civil Engineers: New York, NY, USA, 1971.
24. American Institute of Steel Construction. *Manual of Steel Construction*, 7th ed.; American Institute of Steel Construction: Chicago, IL, USA, 1970.
25. European Committee for Standardization (CEN). *Eurocode 3: Design of Steel Structures—Part 1-1: General Rules and Rules for Buildings*; European Committee for Standardization (CEN): Brussels, Belgium, 1992.
26. Kato, B.; McGuire, W. Analysis of T-stub flange-to-column connections. *J. Struct. Div.* **1973**, *99*, 865–888. [[CrossRef](#)]
27. Packer, J.; LJ, M. A limit state design method for the tension region of bolted beam-column connections. *Struct. Eng.* **1977**, *55*, 446–458.
28. Agerskov, H. Analysis of bolted connections subject to prying. *J. Struct. Div.* **1977**, *103*, 2145–2163. [[CrossRef](#)]
29. Yee, Y.; Melchers, R. Moment-rotation curves for bolted connections. *J. Struct. Eng.* **1986**, *112*, 615–635. [[CrossRef](#)]
30. Astaneh, A. Procedure for design and analysis of hanger-type connections. *Eng. J. AISC* **1985**, *22*, 63–66.
31. Thornton, W.A. Prying action—a general treatment. *Eng. J.* **1985**, *22*, 67–75.
32. Bursi, O.S.; Jaspert, J.P. Calibration of a finite element model for isolated bolted end-plate steel connections. *J. Constr. Steel Res.* **1997**, *44*, 225–262. [[CrossRef](#)]
33. Swanson, J.A.; Kokan, D.S.; Leon, R.T. Advanced finite element modeling of bolted T-stub connection components. *J. Constr. Steel Res.* **2002**, *58*, 1015–1031. [[CrossRef](#)]
34. Girão Coelho, A.M.; Bijlaard, F.S.K.; Simões da Silva, L. Experimental assessment of the ductility of extended end plate connections. *Eng. Struct.* **2004**, *26*, 1185–1206. [[CrossRef](#)]
35. Girão Coelho, A.M. Rotation capacity of partial strength steel joints with three-dimensional finite element approach. *Comput. Struct.* **2013**, *116*, 88–97. [[CrossRef](#)]
36. Abidelah, A.; Bouchaïr, A.; Kerdal, D.E. Influence of the flexural rigidity of the bolt on the behavior of the T-stub steel connection. *Eng. Struct.* **2014**, *81*, 181–194. [[CrossRef](#)]
37. Barata, P.; Ribeiro, J.; Rigueiro, C.; Santiago, A.; Rodrigues, J.P. Assessment of the T-stub joint component at ambient and elevated temperatures. *Fire Saf. J.* **2014**, *70*, 1–13. [[CrossRef](#)]
38. Elfalah, M.; Theofanous, M.; Dirar, S. Behaviour of stainless steel beam-to-column joints—part 2: Numerical modelling and parametric study. *J. Constr. Steel Res.* **2019**, *152*, 194–212. [[CrossRef](#)]
39. Rostami, A.; Moghadam, A.S.; Hosseini, M.; Asghari, N. Evaluation of Formation of Plastic Hinge and Seismic Behavior of Steel Structures Due to Soil–Structure–Tunnel Interaction. *J. Earthq. Tsunami* **2020**, *14*, 2050014. [[CrossRef](#)]
40. Girão Coelho, A.M.; Bijlaard, F.S.K.; Gresnigt, N.; Simões da Silva, L. Experimental assessment of the behaviour of bolted T-stub connections made up of welded plates. *J. Constr. Steel Res.* **2004**, *60*, 269–311. [[CrossRef](#)]
41. Gil, B.; Goñi, R.; Bayo, E. Initial stiffness and strength characterization of minor axis T-stub under out-of-plane bending. *J. Constr. Steel Res.* **2018**, *140*, 208–221. [[CrossRef](#)]
42. Sumner, E.; Mays, T.; Murray, T. *Cyclic Testing of Bolted Moment End-Plate Connections*; Research Report SAC/BD-00/21. CE/VPI-ST 00/03; Department of Civil and Environmental Engineering, Virginia Polytechnic Institute and State University: Blacksburg, VA, USA, 2000.
43. Gerami, M.; Saberi, H.; Saberi, V.; Saedi Daryan, A. Cyclic behavior of bolted connections with different arrangement of bolts. *J. Constr. Steel Res.* **2011**, *67*, 690–705. [[CrossRef](#)]
44. Özkılıç, Y.O. Cyclic and monotonic performance of stiffened extended end-plate connections with large-sized bolts and thin end-plates. *Bull. Earthq. Eng.* **2022**, *20*, 7441–7475. [[CrossRef](#)]
45. Özkılıç, Y.O.; Topkaya, C. Extended end-plate connections for replaceable shear links. *Eng. Struct.* **2021**, *240*, 112385. [[CrossRef](#)]
46. Özkılıç, Y.O. A comparative study on yield line mechanisms for four bolted extended end plated connection. *J. Struct. Mech.* **2021**, *7*, 93–106. [[CrossRef](#)]
47. Özkılıç, Y.O. Investigation of the effects of bolt diameter and end-plate thickness on the capacity and failure modes of end-plated beam-to-column connections. *Res. Eng. Struct. Mater.* **2021**, *7*, 445–463. [[CrossRef](#)]
48. Mistakidis, E.S.; Baniotopoulos, C.C.; Bisbos, C.D.; Panagiotopoulos, P.D. Steel T-Stub connections under static loading: An effective 2-D numerical model. *J. Constr. Steel Res.* **1997**, *44*, 51–67. [[CrossRef](#)]
49. European Commission. *Numerical Aspects for the Simulation of End Plate Connections by the Finite Element Method*; European Commission: Brussels, Belgium, 1999; pp. 13–31.
50. Sherbourne, A.N.; Bahaari, M.R. 3D simulation of bolted connections to unstiffened columns—I. T-stub connections. *J. Constr. Steel Res.* **1996**, *40*, 169–187. [[CrossRef](#)]

51. Bursi, O.S.; Jaspart, J.-P. A refined finite element model for tee-stub and endplate steel connections. In Proceedings of the Giornate Italiane della Costruzione in Acciaio, Riva del Garda, Italy, 15–18 October 1995.
52. Bursi, O.S.; Jaspart, J. Finite element based models for the analysis of bolted beam-to-column steel connections. In Proceedings of the IABSE Colloquium on Semi-Rigid Structural Connections, Istanbul, Turkey, 25–27 September 1996.
53. Bursi, O.S.; Jaspart, J.P. Basic issues in the finite element simulation of extended end plate connections. *Comput. Struct.* **1998**, *69*, 361–382. [[CrossRef](#)]
54. Bursi, O.S.; Jaspart, J.P. Benchmarks for finite element modelling of bolted steel connections. *J. Constr. Steel Res.* **1997**, *43*, 17–42. [[CrossRef](#)]
55. Hantouche, E.; Kukreti, A.; Rassati, G.; Swanson, J. Prying models for strength in thick-flange built-up T-stubs with complete joint penetration and fillet welds. *J. Struct. Eng.* **2015**, *141*, 04014102. [[CrossRef](#)]
56. Hantouche, E.; Kukreti, A.R.; Rassati, G.A. Investigation of secondary prying in thick built-up T-stub connections using nonlinear finite element modeling. *Eng. Struct.* **2012**, *36*, 113–122. [[CrossRef](#)]
57. Hantouche, E.; Kukreti, A.; Rassati, G.; Swanson, J. Modified stiffness model for thick flange in built-up T-stub connections. *J. Constr. Steel Res.* **2013**, *81*, 76–85. [[CrossRef](#)]
58. Hantouche, E.; Abboud, N.H. Stiffness modeling of bolted thick built-up T-stub connections including secondary prying effect. *J. Constr. Steel Res.* **2014**, *95*, 279–289. [[CrossRef](#)]
59. Hantouche, E.; Rassati, G.; Kukreti, A.; Swanson, J. Built-up T-stub connections for moment resisting frames: Experimental and finite element investigation for prequalification. *Eng. Struct.* **2012**, *43*, 139–148. [[CrossRef](#)]
60. Lemonis, M.; Gantes, C. Finite Element Modeling of T-Stub Steel Connections. In Proceedings of the 4th GRACM Congress on Computational Mechanics GRACM, Patras, Greece, 27–29 June 2002.
61. Lemonis, M.; Gantes, C. Numerical analysis of simple and preloaded T-stub steel connections. In *Computational Fluid and Solid Mechanics 2003*; Bathe, K.J., Ed.; Elsevier Science Ltd.: Oxford, UK, 2003; pp. 414–417. [[CrossRef](#)]
62. Gantes, C.J.; Lemonis, M.E. Influence of equivalent bolt length in finite element modeling of T-stub steel connections. *Comput. Struct.* **2003**, *81*, 595–604. [[CrossRef](#)]
63. Lemonis, M.; Gantes, C. Incremental modeling of T-stub connections. *J. Mech. Mater. Struct.* **2006**, *1*, 1135–1159. [[CrossRef](#)]
64. Soltani, R.; Kerdal, D. Behaviour of elementary bolted steel T-stub connections: An evaluation of EC3 design procedure. *Turk. J. Eng. Environ. Sci.* **2011**, *35*, 1–20.
65. Cenicerros, J.F. *Numerical-Informational Methodology for Characterising Steel Bolted Components Coupling Finite Element Simulations and Soft Computing Techniques*; Universidad de La Rioja: Logroño, Spain, 2015.
66. Fernandez-Cenicerros, J.; Sanz-Garcia, A.; Antoñanzas-Torres, F.; Martinez-de-Pison, F.J. A numerical-informational approach for characterising the ductile behaviour of the T-stub component. Part 1: Refined finite element model and test validation. *Eng. Struct.* **2015**, *82*, 236–248. [[CrossRef](#)]
67. Fernandez-Cenicerros, J.; Sanz-Garcia, A.; Antoñanzas-Torres, F.; Martinez-de-Pison, F.J. A numerical-informational approach for characterising the ductile behaviour of the T-stub component. Part 2: Parsimonious soft-computing-based metamodel. *Eng. Struct.* **2015**, *82*, 249–260. [[CrossRef](#)]
68. Kombate, T.J.D.L.C.; Taşkın, K. State-of-the-art review on the behaviour of T-stubs and prying action. *J. Constr. Steel Res.* **2022**, *191*, 107203. [[CrossRef](#)]
69. Bravo, M.A.; Herrera, R.A. Performance under cyclic load of built-up T-stubs for Double T moment connections. *J. Constr. Steel Res.* **2014**, *103*, 117–130. [[CrossRef](#)]
70. Herrera, R.A.; Bravo, M.; Gómez, G.; Aedo, G. Performance of built-up T-stubs for Double T moment connections. *J. Constr. Steel Res.* **2013**, *88*, 289–295. [[CrossRef](#)]
71. Vahdati, V.J.; Yaghoubi, S.; Torabipour, A.; Correia, J.A.F.O.; Fazerer-Ferradosa, T.; Taveira-Pinto, F. Combined solutions to reduce scour around complex foundations: An experimental study. *Mar. Syst. Ocean Technol.* **2020**, *15*, 81–93. [[CrossRef](#)]
72. Ribeiro, J.; Santiago, A.; Rigueiro, C.; Barata, P.; Veljkovic, M. Numerical assessment of T-stub component subjected to impact loading. *Eng. Struct.* **2016**, *106*, 450–460. [[CrossRef](#)]
73. Özkılıç, Y.O.; Topkaya, C. The plastic and the ultimate resistance of four-bolt extended end-plate connections. *J. Constr. Steel Res.* **2021**, *181*, 106614. [[CrossRef](#)]
74. Özkılıç, Y.O. The effects of stiffener configuration on stiffened T-stubs. *Steel Compos. Struct.* **2022**, *44*, 475–488.
75. Özkılıç, Y.O. The capacities of unstiffened T-stubs with thin plates and large bolts. *J. Constr. Steel Res.* **2021**, *186*, 106908. [[CrossRef](#)]
76. Özkılıç, Y.O. The capacities of thin plated stiffened T-stubs. *J. Constr. Steel Res.* **2021**, *186*, 106912. [[CrossRef](#)]
77. Daryan, A.S.; Sadri, M.; Saberi, H.; Saberi, V.; Moghadas, A.B. Behavior of semi-rigid connections and semi-rigid frames. *Struct. Des. Tall Spec. Build.* **2014**, *23*, 210–238. [[CrossRef](#)]
78. Shiravand, M.R.; Torabipour, A.; Mahboubi, S. Parametric Study on Effect of Adding Stiffener to Post-tensioned Steel Connection. *Int. J. Steel Struct.* **2019**, *19*, 478–494. [[CrossRef](#)]
79. Abdollahzadeh, G.; Barchkheil, N.A.; Torabipour, A. Moment–rotation response of post-tensioned self-centring beam–column connection. *Proc. Inst. Civ. Eng. Struct. Build.* **2020**, *173*, 440–457. [[CrossRef](#)]
80. Torabipour, A.; Abdollahi, A.; Yaghoubi, S. Assess the Effectiveness of SMA on Response of Steel Connection with PT Strands. *KSCE J. Civ. Eng.* **2019**, *23*, 5133–5142. [[CrossRef](#)]

81. Maghsoudi, A.; Maghsoudi, M.; Haghighi, H. FE Modeling and Experimental Comparison of RC Beams Consisting Shape Memory Alloys under Cyclic Loading. *Amirkabir J. Civ. Eng.* **2018**, *49*, 745–754. [[CrossRef](#)]
82. Asada, H.; Tanaka, T.; Yamada, S.; Matoba, H. Proposal for seismic retrofit of beam-to-column connection by the addition of H-section haunches to beams using bolt connection. *Int. J. Steel Struct.* **2014**, *14*, 865–871. [[CrossRef](#)]
83. Sebbagh, H.R.; Kerdal, D.E.D.; Abidelah, A.; Bouchaïr, A. T-stubs with two and four bolts under monotonic and cyclic loading. *J. Constr. Steel Res.* **2021**, *178*, 106486. [[CrossRef](#)]
84. Yadupriya, M.C.; Rajeevan, B. Numerical analysis on bolted T-stub to square hollow section connections under tension. 2022. Available online: <https://ssrn.com/abstract=4269427> (accessed on 6 November 2022).
85. Tartaglia, R.; D’Aniello, M.; Zimbru, M. Experimental and numerical study on the T-Stub behaviour with preloaded bolts under large deformations. *Structures* **2020**, *27*, 2137–2155. [[CrossRef](#)]
86. Wang, Y.; Qiao, X.; Jia, L.; Zhang, T.; Jiang, Q. Experimental research on seismic behavior of stainless steel beam-column connections with different link modes. *J. Southeast Univ.* **2018**, *48*, 316–322.
87. Liu, M.; Shi, G. Cyclic loading tests of duplex stainless steel beam-to-column joints with WUF-W connections. In Proceedings of the Ninth International Conference on Advances in Steel Structures (ICASS), Hong Kong, China, 5–7 December 2018; pp. 947–956.
88. Bu, Y.; Wang, Y.; Zhao, Y. Study of stainless steel bolted extended end-plate joints under seismic loading. *Thin-Walled Struct.* **2019**, *144*, 106255. [[CrossRef](#)]
89. Yuan, H.X.; Liu, X.H.; Liu, J.L.; Theofanous, M. Cyclic behaviour and hysteretic model of austenitic stainless steel bolted T-stubs. *J. Constr. Steel Res.* **2021**, *182*, 106659. [[CrossRef](#)]
90. Zhao, M.S.; Lee, C.K.; Chiew, S.P. Tensile behavior of high performance structural steel T-stub joints. *J. Constr. Steel Res.* **2016**, *122*, 316–325. [[CrossRef](#)]
91. Sun, F.F.; Xue, X.Y.; Xiao, Y.; Le, Y.M.; Li, G.Q. Effect of welding and complex loads on the high-strength steel T-stub connection. *J. Constr. Steel Res.* **2018**, *150*, 76–86. [[CrossRef](#)]
92. Wang, Z.Y.; Tizani, W.; Wang, Q.Y. Strength and initial stiffness of a blind-bolt connection based on the T-stub model. *Eng. Struct.* **2010**, *32*, 2505–2517. [[CrossRef](#)]
93. Yang, J.-G.; Lee, S.-K.; Moon, J.-K.; Baek, M.-C. Prediction models for the initial rotational stiffness and ultimate plastic moment for a double split tee connection. *Int. J. Steel Struct.* **2014**, *14*, 213–222. [[CrossRef](#)]
94. SAC Joint Venture. *Protocol for Fabrication, Inspection, Testing, and Documentation of Beam-Column Connection Tests and Other Experimental Specimens*; Rep. No. SAC/BD-97; SAC Joint Venture: Redwood City, CA, USA, 1997; p. 2.
95. Liu, Y.; Málaga-Chuquitaype, C.; Elghazouli, A.Y. Response and component characterisation of semi-rigid connections to tubular columns under axial loads. *Eng. Struct.* **2012**, *41*, 510–532. [[CrossRef](#)]
96. Massimo, L.; Gianvittorio, R.; Aldina, S.; da Silva Luis, S. Experimental analysis and mechanical modeling of T-stubs with four bolts per row. *J. Constr. Steel Res.* **2014**, *101*, 158–174. [[CrossRef](#)]
97. De Matteis, G.; Mandara, A.; Mazzolani, F.M. T-stub aluminium joints: Influence of behavioural parameters. *Comput. Struct.* **2000**, *78*, 311–327. [[CrossRef](#)]
98. Wang, Z.Y.; Wang, Q.-Y. Yield and ultimate strengths determination of a blind bolted endplate connection to square hollow section column. *Eng. Struct.* **2016**, *111*, 345–369. [[CrossRef](#)]
99. Yapici, O.; Theofanous, M.; Yuan, H.; Dirar, S.; Afshan, S. Numerical simulation and design of ferritic stainless steel bolted T-stubs in tension. *J. Constr. Steel Res.* **2022**, *198*, 107555. [[CrossRef](#)]
100. Royal Civil Service Commission. *Specification for Structural Joints Using High-Strength Bolts*; American Institute of Steel Construction: Chicago, IL, USA, 2014.
101. American Institute of Steel Construction. *Specification for Structural Steel Buildings*. In *An American National Standard*; American Institute of Steel Construction: Chicago, IL, USA, 2016.
102. DesRoches, R.; McCormick, J.; Delemont, M. Cyclic properties of superelastic shape memory alloy wires and bars. *J. Struct. Eng.* **2004**, *130*, 38–46. [[CrossRef](#)]
103. Wang, B.; Zhu, S.; Qiu, C.-X.; Jin, H. High-performance self-centering steel columns with shape memory alloy bolts: Design procedure and experimental evaluation. *Eng. Struct.* **2019**, *182*, 446–458. [[CrossRef](#)]
104. Wang, B.; Zhu, S. Cyclic tension–compression behavior of superelastic shape memory alloy bars with buckling-restrained devices. *Constr. Build. Mater.* **2018**, *186*, 103–113. [[CrossRef](#)]
105. Pereiro-Barceló, J.; Bonet, J.L.; Cabañero-Escudero, B.; Martínez-Jaén, B. Cyclic behavior of hybrid RC columns using High-Performance Fiber-Reinforced Concrete and Ni-Ti SMA bars in critical regions. *Compos. Struct.* **2019**, *212*, 207–219. [[CrossRef](#)]
106. Chowdhury, M.A.; Rahmzadeh, A.; Moradi, S.; Alam, M.S. Feasibility of using reduced length superelastic shape memory alloy strands in post-tensioned steel beam–column connections. *J. Intell. Mater. Syst. Struct.* **2019**, *30*, 283–307. [[CrossRef](#)]
107. Özkılıç, Y.O. A new replaceable fuse for moment resisting frames: Replaceable bolted reduced beam section connections. *Steel Compos. Struct.* **2020**, *35*, 353–370. [[CrossRef](#)]
108. Ricles, J.M.; Sause, R.; Garlock, M.M.; Zhao, C. Posttensioned Seismic-Resistant Connections for Steel Frames. *J. Struct. Eng.* **2001**, *127*, 113–121. [[CrossRef](#)]
109. Bozkurt, M.B.; Kazemzadeh Azad, S.; Topkaya, C. Development of detachable replaceable links for eccentrically braced frames. *Earthq. Eng. Struct. Dyn.* **2019**, *48*, 1134–1155. [[CrossRef](#)]

110. Bozkurt, M.B.; Topkaya, C. Replaceable links with direct brace attachments for eccentrically braced frames. *Earthq. Eng. Struct. Dyn.* **2017**, *46*, 2121–2139. [[CrossRef](#)]
111. Bozkurt, M.B.; Topkaya, C. Replaceable links with gusseted brace joints for eccentrically braced frames. *Soil Dyn. Earthq. Eng.* **2018**, *115*, 305–318. [[CrossRef](#)]
112. Özkılıç, Y.O. Optimized stiffener detailing for shear links in eccentrically braced frames. *Steel Compos. Struct. Int. J.* **2021**, *39*, 35–50. [[CrossRef](#)]
113. Özkılıç, Y.O.; Bozkurt, M.B.; Topkaya, C. Mid-spliced end-plated replaceable links for eccentrically braced frames. *Eng. Struct.* **2021**, *237*, 112225. [[CrossRef](#)]
114. Özkılıç, Y.O. Interaction of flange and web slenderness, overstrength factor and proposed stiffener arrangements for long links. *J. Constr. Steel Res.* **2022**, *190*, 107150. [[CrossRef](#)]
115. Korkmaz, H.H.; Dere, Y.; Özkılıç, Y.O.; Bozkurt, M.B.; Ecemiş, A.S.; Özdoner, N. Excessive snow induced steel roof failures in Turkey. *Eng. Fail. Anal.* **2022**, *141*, 106661. [[CrossRef](#)]
116. El-Tawil, S.; Mikesell, T.; Vidarsson, E.; Kunnath, S. *Strength and Ductility of FR Welded-Bolted Connections*; Department of Civil and Environmental Engineering, University of Central Florida: Orlando, FL, USA, 1998; p. 150.
117. Fang, C.; Wang, W.; He, C.; Chen, Y. Self-centring behaviour of steel and steel-concrete composite connections equipped with NiTi SMA bolts. *Eng. Struct.* **2017**, *150*, 390–408. [[CrossRef](#)]
118. Fang, C.; Yam, M.C.H.; Lam, A.C.C.; Xie, L. Cyclic performance of extended end-plate connections equipped with shape memory alloy bolts. *J. Constr. Steel Res.* **2014**, *94*, 122–136. [[CrossRef](#)]
119. Chopra, A.K. *Dynamics of Structures: Theory and Applications to Earthquake Engineering*, 4th ed.; Prentice Hall: Englewood Cliffs, NJ, USA, 2011.
120. He, M.-j.; Liu, H.-f. Comparison of glulam post-to-beam connections reinforced by two different dowel-type fasteners. *Constr. Build. Mater.* **2015**, *99*, 99–108. [[CrossRef](#)]
121. Elmenhawwi, A.; Brown, T. Hysteretic energy and damping capacity of flexural elements constructed with different concrete strengths. *Eng. Struct.* **2010**, *32*, 297–305. [[CrossRef](#)]
122. Speicher, M.S.; DesRoches, R.; Leon, R.T. Experimental results of a NiTi shape memory alloy (SMA)-based recentering beam-column connection. *Eng. Struct.* **2011**, *33*, 2448–2457. [[CrossRef](#)]
123. American Society for Testing and Materials. *Standard Test Methods for Cyclic (Reversed) Load Test for Shear Resistance of Vertical Elements of the Lateral Force Resisting Systems for Buildings*; American Society for Testing and Materials: West Conshohocken, PA, USA, 2019; p. 15.

Disclaimer/Publisher’s Note: The statements, opinions and data contained in all publications are solely those of the individual author(s) and contributor(s) and not of MDPI and/or the editor(s). MDPI and/or the editor(s) disclaim responsibility for any injury to people or property resulting from any ideas, methods, instructions or products referred to in the content.